Fault scarps and tectonic strain in young volcanic seafloor

Jie Chen, Javier Escartin, Mathilde Cannat

▶ **To cite this version:**

Jie Chen, Javier Escartin, Mathilde Cannat. Fault scarps and tectonic strain in young volcanic seafloor. Earth and Planetary Science Letters, 2025, 651, pp.119174. 10.1016/j.epsl.2024.119174 . hal-04833487

HAL Id: hal-04833487
https://hal.science/hal-04833487v1

Submitted on 12 Dec 2024

HAL is a multi-disciplinary open access archive for the deposit and dissemination of scientific research documents, whether they are published or not. The documents may come from teaching and research institutions in France or abroad, or from public or private research centers.

L'archive ouverte pluridisciplinaire **HAL**, est destinée au dépôt et à la diffusion de documents scientifiques de niveau recherche, publiés ou non, émanant des établissements d'enseignement et de recherche français ou étrangers, des laboratoires publics ou privés.

Fault scarps and tectonic strain in young volcanic seafloor

Jie Chen[1,2], Javier Escartin[2], Mathilde Cannat[1]

[1] Université Paris Cité, Institut de physique du globe de Paris, CNRS, 75005 Paris, France

[2] Laboratoire de Géologie, Ecole Normale Supérieure/CNRS UMR 8538, PSL Research University, Paris 75005, France

Corresponding author: Jie Chen (chen@geologie.ens.fr)

Author contributions: J.C. designed the study with J.E. and M.C. J.C. conducted the bathymetric analyses, calculated the apparent tectonic strain, and wrote the paper. All authors discussed the results and reviewed the manuscript.

Keywords: Mid-Ocean Ridge, Autonomous Underwater Vehicle, high-resolution bathymetry, fault scarp, young seafloor, tectonic strain

This PDF file includes:

Highlights

Main Text

Fig. 1 to 5

Highlights:

- Fine-scale faults identified using AUV-borne bathymetry data at 8 MOR seafloor sites
- Apparent tectonic strain (ATS) maps in volcanic young seafloor show high spatial variability
- Fault scarps poorly reflect the tectonic component of plate divergence or the M value
- ATS weakly correlates with spreading rate, melt flux, and thermal regime
- ATS is highly time-dependent, influenced by volcanic eruptions and dike intrusions

Abstract

Fault scarps at Mid-Ocean Ridges (MOR) are recognizable on the seafloor, and often measured to estimate the tectonic component of plate divergence. This estimate, based on linear fault scarp parameters, is referred to here as apparent tectonic strain (ATS). However, ATS may differ from the actual tectonic strain at a lithosphere scale. This is clear at detachment faults at magma-poor slow-ultraslow spreading ridges that do not correspond to linear scarps yet accommodate very high strain. Here we study fault scarps in young volcanic MOR seafloor, using high-resolution (1-2 m) bathymetry data of 8 sites with spreading rates of 14-110 km/Ma. Our results show a weak correlation between ATS and factors such as spreading rate, melt flux, or thermal regime, challenging the use of ATS as a proxy for the MOR tectonic component of plate divergence. Instead, ATS is time-dependent and heterogeneous spatially, controlled by the frequency and size of dike intrusions with associated faults and volcanic eruptions that resurface the seafloor and cover faults. Our findings also have implications for estimates of tectonic extension in subaerial volcanic rifting systems that undergo similar processes.

Introduction

The seafloor formed at Mid-Ocean Ridges (MOR) covers more than 65% of the Earth's surface and is created as a response to plate divergence by the combination of magmatic accretion and tectonic extension. Magmatic accretion occurs through dike intrusions and seafloor eruptions in the upper crust and melt crystallization in the lower crust (Detrick et al., 1987; Sinton and Detrick, 1992). The tectonic component of plate divergence is taken up by slip along normal faults that develop and grow within the brittle lithosphere (Buck et al., 2005; Carbotte and Macdonald, 1994). The contribution of magmatic accretion, often denoted as the M value (Behn and Ito, 2008; Buck et al., 2005; Ito and Behn, 2008; Liu and Buck, 2020; Olive and Dublanchet, 2020), is a key parameter for MOR processes, which has predictable consequences in terms of seafloor spreading modes, axial thermal regimes, magnetic patterns, and hydrothermal circulation (Cannat et al., 2006; Chen et al., 2023a; Zhou and Dyment, 2023).

As the quantification of the magmatic component of plate divergence is challenging, in practice, researchers have proposed quantifications for the apparent tectonic component (i.e., 1-M value) by summing the heaves of linear fault scarps at the seafloor and calculating the corresponding % value of total plate divergence based on local spreading rates and the width of the study area (Bohnenstiehl and Carbotte, 2001; Carbotte and Macdonald, 1994; Chen et al., 2021; Combier et al., 2015; Cowie et al., 1994; Deschamps et al., 2007; Escartín et al., 2007, 1999; Howell et al., 2016; Le Saout et al., 2018, 2023; Olive et al., 2024). As this approach is based on measuring linear fault scarps that are apparent on the seafloor (i.e., tectonic deformation in depth is not accounted), we will refer to the resulting values as apparent tectonic strain (ATS), or apparent tectonic component of plate divergence, and examine its potential as a proxy to measure actual MOR tectonic components.

At fast-spreading ridges, plate divergence is dominated by magmatic accretion; ATS is commonly below 5% (Bohnenstiehl and Carbotte, 2001; Carbotte and Macdonald, 1994; Cowie et al., 1994; Escartín et al., 2007; Le Saout et al., 2018; Wu et al., 2023), and most near-axis faults likely form due to local stresses induced by diking (Le Saout et al., 2018; Soule et al., 2009). At slow-spreading ridges, plate divergence comprises a more significant component of tectonic extension, resulting over timescales of several hundred thousand years in the formation of axial valleys (Ito and Behn, 2008; Small, 1998). At melt-poor ridge sections, long-offset detachment faults do not produce linear scarps yet contribute between 50% to nearly 100% of the total plate divergence over long periods (MacLeod et al., 2009;

Sauter et al., 2013). In contrast, young volcanic seafloor at melt-rich slow and ultraslow ridge sections yields ATS values between 2 and 16% (Chen et al., 2021; Combier et al., 2015; Escartín et al., 1999; Le Saout et al., 2023), similar to or larger than those at fast ridges. The young seafloor in these volcanically active regions is a critical zone where faults nucleate and may evolve to prominent axial valley walls and off-axis abyssal hills. Yet, similar to fast ridges, faults there interact with volcanism and mass wasting (Fig. 1a), at different temporal and spatial scales that may depend on spreading rate, resulting in ATS values probably different from the actual tectonic component.

High-resolution bathymetry data and fault detection

Most ATS studies cited above have used shipboard bathymetry data with a resolution (20-100 m; Fig. S1a) that is insufficient to identify smaller faults. High-resolution (HR; 1-2 m) bathymetry data collected by state-of-art Autonomous Underwater Vehicle (AUV) and Remotely Operated Vehicle (ROV) revolutionizes our ability to map fine-scale volcanic and tectonic features on the seafloor (Chen et al., 2021; Le Saout et al., 2018; Wu et al., 2023).

ATS studies using such HR bathymetry data have been published for several sites at young volcanic seafloor from fast to ultraslow spreading ridges, such as the 9°N (Wu et al., 2023) (Fig. 2a) and the 16°N (Le Saout et al., 2018) of the East Pacific Ridge (EPR), the Explorer region (Deschamps et al., 2007) (Fig. 2b) of the Juan de Fuca Ridge (JdFR), and the 50.5°E region (Chen et al., 2021) (Fig. 2h) of the Southwest Indian Ridge (SWIR). However, none of these studies proposed a global comparison. Here, we study young volcanic seafloor at 8 MOR sites over a broad range of spreading rates (14-110 km/Ma), using a compilation of available HR bathymetry data covering a total area of 400 km^2 (all standardized to the same distance scale and the same relative color scale in Fig. 2a-2h). Estimated maximum and mean crustal ages at these sites range between ~50 and ~940 kyr, and between ~30 and ~590 kyr, respectively (Methods and Table S1 in Supplementary). The meaning of our ATS values is, therefore, different from those measured on off-axis older seafloor associated with more mature faults (Carbotte and Macdonald, 1994; Escartín et al., 1999; Howell et al., 2016; Olive et al., 2024). As a result, we identified 9188 faults and fissures in total (1833 km in length), which are used to 1) quantify ATS with a novel approach to highlight its spatial variability, 2) explore the relation between the ATS and the actual tectonic component of plate divergence, and 3) propose a conceptual synthesis of fault evolution in young volcanic

seafloor over the full range of spreading rates, considering the interplay between tectonic, volcanic, and mass-wasting processes over different temporal and spatial scales.

Apparent tectonic strain

In most previous works, apparent tectonic strain (ATS) is calculated by summing the heave (based on the measurements of fault relief and dip) of ridge-parallel faults and the width of fissures, along a few selected (or regularly spaced) cross-axis transects. This approach has been applied to HR bathymetry data by researchers (Chen et al., 2021; Deschamps et al., 2007; Wu et al., 2023) in 3 of the 8 study sites considered here (i.e., EPR 9°N, Explorer, and SWIR 50.5°E; estimated ATS values in Table S1). With this approach, it is difficult to evaluate the spatial variability of ATS along and across the ridge axis. To characterize this spatial variability and ultimately link it to other processes like volcanism, we calculate the map of *ATS* based on the fault heave (*H*) and fissure width (*W*) over a given area. We calculate fault heave from measured fault relief (*R;* Fig. 1a) along cross-axis transects spaced at C = 2 m (see Methods in Supplementary), applying a circular window expressed as:

$$\Sigma H = \frac{\Sigma R}{tan(\alpha)},$$
$$ATS = 100\% \times C \cdot (\Sigma H + \Sigma W) \,/\, \pi r^2,$$

where r is the search radius of the moving circular window, ΣR, ΣH, and ΣW are accumulations of fault relief, fault heave, and fissure width within the search window, respectively, and α is the fault dip inferred here, as in previous studies (Chen et al., 2021; Deschamps et al., 2007; Le Saout et al., 2018), to have a uniform value.

To do so, we picked closed polygons of all apparent fault scarps and fissures for the 8 study sites (see Methods in Supplementary). The cumulative frequency of the maximum fault relief of each site follows an exponential law (see log-linear plots in Fig. S4), suggesting that our picking process correctly records small fault scarps down to 2-4 m. The search radius (r) is constrained by the fault spacing measured along 2-m-spaced cross-axis transects; across the 8 study sites, the average fault spacing is 180 m, with variations among individual study sites ranging from 71 to 577 m (Table S1). The fault dip (α) is constrained by the median value of the fault dip versus fault throw stabilizing at 60-75° at throws of >50 m (Fig. S5). To evaluate the robustness of our ATS calculation, we use the combination of r = 200 m and α = 65° in Fig. 3 and Fig. 4, and test other combinations of r (100 and 400 m) and α (75°) in Fig. S6-S14.

Fig. 3 shows maps of seafloor morphology, faulting pattern, and ATS of three sites with extensive coverage of HR bathymetry data (Fig. 2i): the fast-spreading EPR 9°N (110 km/Ma) with data covering the axial high (Wu et al., 2023); the intermediate-spreading Endeavour of the JdFR (56 km/Ma) with data covering the axial inflated portion (Clague et al., 2014); and the ultraslow-spreading SWIR 50.5°E (14 km/Ma) with data covering two successive constructions of inflated axial domal volcanos (Chen et al., 2021). Based on our ATS maps, at the EPR 9°N (Fig. 3a), 85% of the young seafloor is nearly fracture-free with ATS <1% (Fig. 4a). This includes the area covered by the 2005-2006 volcanic eruption (Soule et al., 2007). ATS reaches 10% around the first pair of conjugate bounding faults (2-4 km away from the axial high summit). At the Endeavour area (Fig. 3b), faults and fissures concentrate within the graben that rifts the most inflated portion of the axis to a width of 1-2 km, resulting in local ATS values up to 20-25% (e.g., the rifted seamount near 48°N). Outside this axial graben, the seafloor is fracture-free with nearly-zero ATS. At the SWIR 50.5°E (Fig. 3c), the seafloor is extensively faulted, lacking a continuous volcanic or tectonic axis. There are three ridge-parallel fracture-free stripes (i.e., nearly-zero ATS): the smooth lava flow surrounding the northern bounding fault system (NF1), the recent hummocky lava flows built by multiple eruptions, and the smooth lava flow region in the southernmost part of the mapped area (Chen et al., 2021). Between these fracture-free stripes, ATS reaches up to >20%.

The other five study sites (see Fig. S9-S13) include the Explorer area (60 km/Ma) of the JdFR, similar to the Endeavour area, that has concentrated faulting within the axial graben with ATS of up to 24% (Fig. S9). At the 92°W (55 km/Ma) and 95°W (53 km/Ma) regions of the intermediate-spreading Galapagos Spreading Center (GSC), with data covering the axial high and the bottom of the axial valley, respectively, local ATS values vary between 0 and 18% (Fig. S10 and S11). At the 14°N (27 km/Ma) region of slow-spreading Mid-Atlantic Ridge (MAR), data covers the entire 9-km-wide axial valley, and local ATS values vary between >40% near the valley wall and nearly-zero in the youngest seafloor (Fig. S12). At the Lucky Strike area (21 km/Ma) of the MAR, local ATS values peak over the inflated domal volcano at the segment center (>20%) and decrease toward the segment end (<1%) (Fig. S13). We also compare with a fault study at the EPR 16°N (85 km/Ma) using HR (1 m) bathymetry data, which illustrates an along-axis variation of ATS between 1.4 and 6.4% assuming a uniform fault dip of 65°, measured along five cross-axis transects spaced at 2 km (Le Saout et al., 2018).

169 Therefore, there are large variations of ATS within each study site at local spatial scales.
170 To convey this local variability in faulting, and in the associated ATS values, Fig. 4a shows
171 both the range and the frequency distribution of ATS for the 8 study sites. Overall, most of
172 the mapped seafloor (280 km^2 out of the total 400 km^2) displays ATS of <4%, and only a
173 small portion of the seafloor (55 km^2) exhibits ATS exceeding 8%. These values are nearly
174 independent of the given search radius (Fig. S14a and S14b).

175 **Fault scarps in young seafloor poorly reflect the tectonic component of plate divergence**

176 It is widely hypothesized that the tectonic component of plate divergence decreases with
177 the increases in spreading rate and melt flux (the product of spreading rate and magmatic
178 crustal thickness) (Behn and Ito, 2008; Olive and Dublanchet, 2020; Shaw and Lin, 1996).
179 We integrate our observations and previous geophysical studies at the 8 study sites, together
180 with the EPR 16°N where apparent tectonic strain (ATS) averages 2.7% based on five cross-
181 axis transects (Le Saout et al., 2018). The average ATS of the 8 study sites (calculated using
182 all faults and fissures within the mapped area) is lowest at the fastest-spreading, highest-melt-
183 flux study site (EPR 9°N), but others show no clear correlation with spreading rate and
184 inferred melt flux (Fig. 4b-4c and data listed in Table S1). There is, however, a broader range
185 of both the average ATS values and the local ATS variability for study sites at intermediate
186 to slow spreading rates and melt fluxes (Fig. 4). At the scale of a given study area, the
187 relation between ATS and melt flux may even be opposite to predictions: for example, the
188 inflated domal volcano in the center of the Lucky Strike area, where the local melt flux is
189 highest, displays the highest local ATS (Fig. S13c), possibly reflecting the variations from
190 localized deformation at a narrow graben within the rift valley, to distributed deformation
191 throughout the full width of the rift valley floor, from the center to the end of the Lucky
192 Strike segment.

193 This overall lack of a correlation, or in some cases correlations that go against common
194 expectations, means that parameters beyond spreading rate and melt flux also affect ATS
195 values. The depth of the axial melt lens (AML), when present, may be one such parameter
196 because it represents a lower bound for the thickness of the axial lithosphere and, therefore,
197 could be expected to correlate with axial faulting characteristics. However, we show that
198 AML depth is not correlated either with ATS values (Fig. 4b). AML depths are similar at
199 EPR 9°N and 16°N (~1.5 km below the seafloor; (Carbotte et al., 1998; Marjanović et al.,
200 2014), yet the average ATS at the EPR 16°N (Le Saout et al., 2018) is >4 times higher than

that of the EPR 9°N (2.7% vs. 0.59%; Fig. 4b). At the intermediate-spreading GSC, the 92°W area has a higher melt flux and a shallow AML (1.4 km), while the 95°W area does not have a crustal AML (Blacic et al., 2004), yet their average ATS values are close (~2%; Fig. 4b and 4c). At the intermediate-spreading JdFR, the Endeavour area has a 2.1-km deep AML (Arnoux et al., 2019; Carbotte et al., 2006) and an average ATS value of 5.4% (Fig. 4b) that is ~1.8 times higher than that of the slow- and ultraslow-spreading Lucky Strike and SWIR 50.5°E areas where the AML and/or seismic low-velocity anomaly (LVA) are significantly deeper (3-4 km) (Li et al., 2015; Singh et al., 2006).

These comparisons demonstrate that fault scarps in young volcanic seafloor do not accurately reflect the long-term, lithospheric-scale tectonic component of plate divergence. ATS values are, therefore, not appropriate for estimating the M value at any MOR locations. The hypothesis we make here is that faulting characteristics and the resulting ATS values are also strongly affected by two types of volcanic processes. The first volcanic process reduces ATS values and is simply that lava flows may bury pre-existing fault scarps. This is typically the case with high-effusion-rate smooth lava flows that have been documented to cover the seafloor up to 2 km from the eruptive source (Chen et al., 2021; Soule et al., 2007). At the EPR 9°N, fault scarps in young seafloor are presumably buried by lavas from eruptions that occurred as recently as 2005-2006 (Escartín et al., 2007; Soule et al., 2007); while at slow-spreading centers, these scarps may steer flows that partially cover these scarps (Gini et al., 2021). At the SWIR 50.5°E area, several eruptions of smooth lava flow that occurred over the past 780 kyrs also lead to fracture-free stripes (Chen et al., 2021) (Fig. 3c). The second volcanic process increases ATS values and involves the formation of linear normal fault scarps in response to dikes stalling at depth and not reaching to the seafloor (Chadwick and Embley, 1998; Rubin, 1992). At the EPR 9°N and 16°N, it has been proposed that most faults in the axial summit trough region originate that way (Le Saout et al., 2018; Soule et al., 2009). Locally high ATS values in volcanically-robust portions of intermediate-slow-ultraslow ridges (i.e., the Endeavour, Explorer, Lucky Strike, and SWIR 50.5°E study areas) could also be explained by frequent dike intrusions, if a significant proportion does not result in eruptions (Gudmundsson and Brenner, 2004; Hooft et al., 1996).

In Fig. S15, we also estimate the average ATS rates of the 8 study sites and the EPR 16°N by dividing the average ATS values by mean crustal ages, yielding a range from 3×10^{-8} to 2.5×10^{-6} yr^{-1}. However, uncertainties must be considered in these estimates, particularly those related to the inherited use of general and uniform spreading rates in axial regions (see

Methods in Supplementary), which is beyond the scope of this paper that focuses on small-scale temporal and spatial variability of faulting.

A synthesis of fault evolution in young seafloor

Fault scarps across all spreading rates should grow over time if evolving only in response to tectonic extension. The high temporal and spatial variability in apparent tectonic strain (ATS) is therefore interpreted here as primarily related to volcanic eruptions and/or dike injections (Fig. 5a). In young volcanic seafloor, a high apparent tectonic strain could result from a high tectonic component of plate divergence (i.e., a low M value) and/or a high frequency of dike injections, combined with an overall low eruption rate. However, we do not deal with detachment faults at magma-poor slow-ultraslow spreading ridges that accommodate very high strain (up to 50-100%).

We, therefore, should be cautious when comparing the temporal and spatial variability of ATS at different spreading rates and melt fluxes, for example, between the EPR 9°N, the Endeavour, and the SWIR 50.5°E study sites (spreading rates of 110, 56, and 14 km/Ma, respectively; Fig. 5b, 5c, and 5d). At a given area, the seafloor at the SWIR 50.5°E records a history that is about 8 and 4 times longer than that of the EPR 9°N and the Endeavour, respectively. The interval of volcanic eruptions at the EPR 9°N is only tens of years (Perfit and Chadwick, 1998; Soule et al., 2007). It is probably 1 to 3 orders of magnitude higher for the Endeavour and the SWIR 50.5°E (Perfit and Chadwick, 1998). The seafloor at the EPR 9°N is, therefore, more frequently resurfaced by lava flows. Eruptions are also discrete events in time and space, and the spatial extent of volcanic eruptions is mainly influenced by lava effusion rates (Chen et al., 2021). A high lava-effusion-rate eruption produces extensive lava flows efficiently covering seafloor (e.g., the 2005-2006 eruption at the EPR 9°N in Fig. 5b), and a low lava-effusion-rate eruption produces patchy hummocky cones/ridges covering seafloor around the eruptive source (e.g., the recent hummocky eruption at the SWIR 50.5°E in Fig. 5d). In all cases, lava-buried faults may be reactivated by subsequent tectonic or dike-induced deformation.

Dike-induced faults can also vary temporally and spatially, influenced by factors such as the axial thermal regime, the frequency of dike injections, and the length and depth of intrusion. At fast spreading ridges, a shallow magma chamber (~1.5 km below the seafloor) is an ideal setting to develop dike-induced faults, as the brittle lid is relatively weak and thin. For example, at the EPR 9°N, this setting leads to the development of the axial summit

trough and the nucleation of asymmetric faults outside the trough (Marjanović et al., 2024; Soule et al., 2009); faults can be induced by the formation of new AMLs, while melt may be transported into existing faults to trigger eruptions, resulting in a fluctuating rate of apparent fault growth over short timescales. As dike-induced faults typically form symmetrically about the dike (Chadwick and Embley, 1998; Rubin, 1992), continuous high-frequency dike intrusions with a low proportion of associated eruptions would limit resurfacing but facilitate the development of the axial graben, such as at the Endeavour area (Fig. 5c). As the new seafloor moves away from active axial volcanic systems, faults may grow responding to far-field tectonic stretching, e.g., the paired valley-wall faults in the MAR 14°N area (Fig. 2f and S12) that are typical of volcanic slow-ultraslow spreading ridges.

Furthermore, our interpretation of the faulting patterns and ATS values in young volcanic seafloor, summarized in Fig. 5a, may be applicable to subaerial volcanic centers. For example, the East African rift system and the Iceland volcanic system display significant along-rift variations in faulting patterns and ATS (Corti et al., 2021; Dumont et al., 2019; Siegburg et al., 2020), attributable to this spatial variability in tectonic and volcanic interactions. Similarly, volcanic centers there often correspond to a relatively high ATS, coinciding with recent feeder dikes (Acocella and Trippanera, 2016; Dumont et al., 2019; Grandin et al., 2010). Volcanic deposits can also fully or partially cover fault scarps (Siegburg et al., 2020), thus lowering the apparent fault offset and hence, the ATS, as we observe at mid-ocean ridges.

Acknowledgments

This work was supported by ANR project "Ridge Factory Slow" (ANR- 18-CE01-000201). Jie Chen was funded by Naturalia & Biologia. Figures are generated using GMT-6 (https://www.generic-mapping-tools.org/). This is IPGP contribution #4282.

Data availability

Bathymetry data can be found in the following links: EPR9°N (https://doi.org/10.26022/IEDA/330373), Endeavour (https://doi.org/10.1594/IEDA/321996), GSC 92°W and 95°W (https://doi.org/10.1594/IEDA/318210), MAR 14°N (https://doi.org/10.26022/IEDA/330198), Lucky Strike (https://doi.org/10.17882/80574), and SWIR 50.5°E (https://doi.org/10.5281/zenodo.5147241). All digital faults and fissures and calculated grid files of apparent tectonic strain of all sites can be found in https://figshare.com/s/fe560f15dfe5b3f7c6c7.

References

Acocella, V., Trippanera, D., 2016. How diking affects the tectonomagmatic evolution of slow spreading plate boundaries: Overview and model. Geosphere 12, 867–883. https://doi.org/10.1130/GES01271.1

Arnoux, G.M., Toomey, D.R., Hooft, E.E.E., Wilcock, W.S.D., 2019. Seismic Imaging and Physical Properties of the Endeavour Segment: Evidence that Skew Between Mantle and Crustal Magmatic Systems Governs Spreading Center Processes. Geochemistry, Geophys. Geosystems 20, 1319–1339. https://doi.org/10.1029/2018GC007978

Behn, M.D., Ito, G., 2008. Magmatic and tectonic extension at mid-ocean ridges: 1. Controls on fault characteristics. Geochemistry, Geophys. Geosystems 9, 8–10. https://doi.org/10.1029/2008GC001965

Blacic, T.M., Ito, G., Canales, J.P., Detrick, R.S., Sinton, J., 2004. Constructing the crust along the Galapagos Spreading Center 91.3°-95.5°W: Correlation of seismic layer 2A with axial magma lens and topographic characteristics. J. Geophys. Res. Solid Earth 109, B10310. https://doi.org/10.1029/2004JB003066

Bohnenstiehl, D.W.R., Carbotte, S.M., 2001. Faulting patterns near 19°30′S on the East Pacific Rise: Fault formation and growth at a superfast spreading center. Geochemistry, Geophys. Geosystems 2, 1056. https://doi.org/10.1029/2001GC000156

Buck, W.R., Lavier, L.L., Poliakov, A.N.B., 2005. Modes of faulting at mid-ocean ridges. Nature 434, 719–723. https://doi.org/10.1038/nature03358

Cannat, M., Sauter, D., Mendel, V., Ruellan, E., Okino, K., Escartin, J., Combier, V., Baala, M., 2006. Modes of seafloor generation at a melt-poor ultraslow-spreading ridge. Geology 34, 605–608. https://doi.org/10.1130/G22486.1

Carbotte, S., Mutter, C., Mutter, J., Ponce-Correa, G., 1998. Influence of magma supply and spreading rate on crustal magma bodies and emplacement of the extrusive layer: insights from the East Pacific Rise at lat 16°N. Geology 26, 455–458. https://doi.org/10.1130/0091-7613(1998)026<0455:IOMSAS>2.3.CO;2

Carbotte, S.M., Detrick, R.S., Harding, A., Canales, J.P., Babcock, J., Kent, G., Van Ark, E., Nedimovic, M., Diebold, J., 2006. Rift topography linked to magmatism at the intermediate spreading Juan de Fuca Ridge. Geology 34, 209–212. https://doi.org/10.1130/G21969.1

Carbotte, S.M., Macdonald, K.C., 1994. Comparison of seafloor tectonic fabric at intermediate, fast, and super fast spreading ridges: Influence of spreading rate, plate

motions, and ridge segmentation on fault patterns. J. Geophys. Res. Solid Earth 99, 13609–13631. https://doi.org/10.1029/93jb02971

Chadwick, W.W., Embley, R.W., 1998. Graben formation associated with recent dike intrusions and volcanic eruptions on the mid-ocean ridge. J. Geophys. Res. Solid Earth 103, 9807–9825. https://doi.org/10.1029/97jb02485

Chen, J., Cannat, M., Tao, C., Sauter, D., Munschy, M., 2021. 780 Thousand Years of Upper-Crustal Construction at a Melt-Rich Segment of the Ultraslow Spreading Southwest Indian Ridge 50°28′E. J. Geophys. Res. Solid Earth 126, e2021JB022152. https://doi.org/10.1029/2021JB022152

Chen, J., Olive, J.A., Cannat, M., 2023a. Beyond spreading rate: Controls on the thermal regime of mid-ocean ridges. Proc. Natl. Acad. Sci. 120, e2306466120. https://doi.org/10.1073/pnas.2306466120

Chen, J., Zhang, T., Tominaga, M., Escartin, J., Kang, R., 2023b. Ocean Sciences with the Spilhaus Projection: A Seamless Ocean Map for Spatial Data Recognition. Sci. Data 10, 410. https://doi.org/10.1038/s41597-023-02309-6

Clague, D.A., Dreyer, B.M., Paduan, J.B., Martin, J.F., Caress, D.W., Gill, J.B., Kelley, D.S., Thomas, H., Portner, R.A., Delaney, J.R., Guilderson, T.P., McGann, M.L., 2014. Eruptive and tectonic history of the Endeavour Segment, Juan de Fuca Ridge, based on AUV mapping data and lava flow ages. Geochemistry, Geophys. Geosystems 15, 3364–3391. https://doi.org/10.1002/2014GC005415

Combier, V., Seher, T., Singh, S.C., Crawford, W.C., Cannat, M., Escartín, J., Dusunur, D., 2015. Three-dimensional geometry of axial magma chamber roof and faults at Lucky Strike volcano on the Mid-Atlantic Ridge. J. Geophys. Res. Solid Earth 120, 5379–5400. https://doi.org/10.1002/2015JB012365

Corti, N., Bonali, F.L., Mariotto, F.P., Tibaldi, A., Russo, E., Hjartardóttir, Á.R., Einarsson, P., Rigoni, V., Bressan, S., 2021. Fracture kinematics and holocene stress field at the krafla rift, northern iceland. Geosci. 11, 1–27. https://doi.org/10.3390/geosciences11020101

Cowie, P.A., Malinverno, A., Ryan, W.B.F., Edwards, M.H., 1994. Quantitative fault studies on the East Pacific Rise: a comparison of sonar imaging techniques. J. Geophys. Res. 99, 15205. https://doi.org/10.1029/94jb00041

Deschamps, A., Tivey, M., Embley, R.W., Chadwick, W.W., 2007. Quantitative study of the deformation at Southern Explorer Ridge using high-resolution bathymetric data. Earth Planet. Sci. Lett. 259, 1–17. https://doi.org/10.1016/j.epsl.2007.04.007

365 Detrick, R.S., Buhl, P., Vera, E., Mutter, J., Orcutt, J., Madsen, J., Brocher, T., 1987. Multi-
366 channel seismic imaging of a crustal magma chamber along the East Pacific Rise.
367 Nature 326, 35–41. https://doi.org/10.1038/326035a0
368 Dumont, S., Klinger, Y., Socquet, A., Escartín, J., Grandin, R., Jacques, E., Medynski, S.,
369 Doubre, C., 2019. Rifting Processes at a Continent-Ocean Transition Rift Revealed by
370 Fault Analysis: Example of Dabbahu-Manda-Hararo Rift (Ethiopia). Tectonics 38, 190–
371 214. https://doi.org/10.1029/2018TC005141
372 Dunn, R.A., Toomey, D.R., Solomon, S.C., 2000. Three-dimensional seismic structure and
373 physical properties of the crust and shallow mantle beneath the East Pacific Rise at
374 9°30'N. J. Geophys. Res. Solid Earth 105, 23537–23555.
375 https://doi.org/10.1029/2000jb900210
376 Escartín, J., Cowie, P.A., Searle, R.C., Allerton, S., Mitchell, N.C., MacLeod, C.J., Slootweg,
377 A.P., 1999. Quantifying tectonic strain and magmatic accretion at a slow spreading ridge
378 segment, Mid-Atlantic Ridge, 29°N. J. Geophys. Res. Solid Earth 104, 10421–10437.
379 https://doi.org/10.1029/1998jb900097
380 Escartín, J., Soule, S.A., Fornari, D.J., Tivey, M.A., Schouten, H., Perfit, M.R., 2007.
381 Interplay between faults and lava flows in construction of the upper oceanic crust: The
382 East Pacific Rise crest 9°25′–9°58′N. Geochemistry, Geophys. Geosystems 8, Q06005.
383 https://doi.org/10.1029/2006GC001399
384 Gini, C., Escartín, J., Cannat, M., Barreyre, T., 2021. Extrusive upper crust formation at
385 slow-spreading ridges: Fault steering of lava flows. Earth Planet. Sci. Lett. 576, 117202.
386 https://doi.org/10.1016/j.epsl.2021.117202
387 Grandin, R., Socquet, A., Doin, M.P., Jacques, E., De Chabalier, J.B., King, G.C.P., 2010.
388 Transient rift opening in response to multiple dike injections in the Manda Hararo rift
389 (Afar, Ethiopia) imaged by time-dependent elastic inversion of interferometric synthetic
390 aperture radar data. J. Geophys. Res. Solid Earth 115, B09403.
391 https://doi.org/10.1029/2009JB006883
392 Gudmundsson, A., Brenner, S.L., 2004. Local stresses, dyke arrest and surface deformation
393 in volcanic edifices and rift zones. Ann. Geophys. 47, 1433–1454.
394 https://doi.org/10.4401/ag-3352
395 Hooft, E.E.E., Schouten, H., Detrick, R.S., 1996. Constraining crustal emplacement processes
396 from the variation in seismic layer 2A thickness at the East Pacific Rise. Earth Planet.
397 Sci. Lett. 142, 289–309. https://doi.org/10.1016/0012-821x(96)00101-x
398 Howell, S.M., Ito, G., Behn, M.D., Martinez, F., Olive, J.-A., Escartín, J., 2016. Magmatic

399 and tectonic extension at the Chile Ridge: Evidence for mantle controls on ridge
400 segmentation. Geochemistry, Geophys. Geosystems 17, 2354–2373.
401 https://doi.org/10.1002/2016GC006380
402 Ito, G., Behn, M.D., 2008. Magmatic and tectonic extension at mid-ocean ridges: 2. Origin of
403 axial morphology. Geochemistry, Geophys. Geosystems 9, 9–12.
404 https://doi.org/10.1029/2008GC001970
405 Karson, J.A., Hurst, S.D., Lonsdale, P., 1992. Tectonic rotations of dikes in fast-spread
406 oceanic crust exposed near Hess Deep. Geology 20, 685–688.
407 https://doi.org/10.1130/0091-7613(1992)020<0685:TRODIF>2.3.CO;2
408 Le Saout, M., Pałgan, D., Devey, C.W., Lux, T.S., Petersen, S., Thorhallsson, D.,
409 Tomkowicz, A., Brix, S., 2023. Variations in Volcanism and Tectonics Along the
410 Hotspot-Influenced Reykjanes Ridge. Geochemistry, Geophys. Geosystems 24,
411 e2022GC010788. https://doi.org/10.1029/2022GC010788
412 Le Saout, M., Thibaud, R., Gente, P., 2018. Detailed Analysis of Near Tectonic Features
413 Along the East Pacific Rise at 16°N, Near the Mathematician Hot Spot. J. Geophys. Res.
414 Solid Earth 123, 4478–4499. https://doi.org/10.1029/2017JB015301
415 Li, J., Jian, H., Chen, Y.J., Singh, S.C., Ruan, A., Qiu, X., Zhao, M., Wang, X., Niu, X., Ni,
416 J., Zhang, J., 2015. Seismic observation of an extremely magmatic accretion at the
417 ultraslow spreading Southwest Indian Ridge. Geophys. Res. Lett. 42, 2656–2663.
418 https://doi.org/10.1002/2014GL062521
419 Liu, Z., Buck, W.R., 2020. Global Trends of Axial Relief and Faulting at Plate Spreading
420 Centers Imply Discrete Magmatic Events. J. Geophys. Res. Solid Earth 125,
421 e2020JB019465. https://doi.org/10.1029/2020JB019465
422 MacLeod, C.J., Searle, R.C., Murton, B.J., Casey, J.F., Mallows, C., Unsworth, S.C.,
423 Achenbach, K.L., Harris, M., 2009. Life cycle of oceanic core complexes. Earth Planet.
424 Sci. Lett. 287, 333–344. https://doi.org/10.1016/j.epsl.2009.08.016
425 Marjanović, M., Carbotte, S.M., Carton, H., Nedimović, M.R., Mutter, J.C., Canales, J.P.,
426 2014. A multi-sill magma plumbing system beneath the axis of the East Pacific Rise.
427 Nat. Geosci. 7, 825–829. https://doi.org/10.1038/ngeo2272
428 Marjanović, M., Chen, J., Escartín, J., Parnell-Turner, R., Wu, J.-N., 2024. Magma-induced
429 tectonics at the East Pacific Rise 9°50'N: Evidence from high-resolution
430 characterization of seafloor and subseafloor. Proc. Natl. Acad. Sci. 121, e2401440121.
431 https://doi.org/10.1073/pnas.2401440121
432 Olive, J.A., Dublanchet, P., 2020. Controls on the magmatic fraction of extension at mid-

ocean ridges. Earth Planet. Sci. Lett. 549, 116541. https://doi.org/10.1016/j.epsl.2020.116541

Olive, J.A., Ekström, G., Buck, W.R., Liu, Z., Escartín, J., Bickert, M., 2024. Mid-ocean ridge unfaulting revealed by magmatic intrusions. Nature 628, 782–787. https://doi.org/10.1038/s41586-024-07247-w

Pagli, C., Wang, H., Wright, T.J., Calais, E., Lewi, E., 2014. Current plate boundary deformation of the Afar rift from a 3-D velocity field inversion of InSAR and GPS. J. Geophys. Res. Solid Earth 119, 8562–8575. https://doi.org/10.1002/2014JB011391

Perfit, M.R., Chadwick, W.W., 1998. Magmatism at mid-ocean ridges: Constraints from volcanological and geochemical investigations. Geophys. Monogr. Ser. 106, 59–115. https://doi.org/10.1029/GM106p0059

Rubin, A.M., 1992. Dike-induced faulting and graben subsidence in volcanic rift zones. J. Geophys. Res. 97, 1839–1858. https://doi.org/10.1029/91JB02170

Sauter, D., Cannat, M., Rouméjon, S., Andreani, M., Birot, D., Bronner, A., Brunelli, D., Carlut, J., Delacour, A., Guyader, V., MacLeod, C.J., Manatschal, G., Mendel, V., Ménez, B., Pasini, V., Ruellan, E., Searle, R., 2013. Continuous exhumation of mantle-derived rocks at the Southwest Indian Ridge for 11 million years. Nat. Geosci. 6, 314–320. https://doi.org/10.1038/ngeo1771

Shaw, W.J., Lin, J., 1996. Models of ocean ridge lithospheric deformation: Dependence on crustal thickness, spreading rate, and segmentation. J. Geophys. Res. Solid Earth 101, 17977–17993. https://doi.org/10.1029/96jb00949

Siegburg, M., Bull, J.M., Nixon, C.W., Keir, D., Gernon, T.M., Corti, G., Abebe, B., Sanderson, D.J., Ayele, A., 2020. Quantitative Constraints on Faulting and Fault Slip Rates in the Northern Main Ethiopian Rift. Tectonics 39, e2019TC006046. https://doi.org/10.1029/2019TC006046

Singh, S.C., Crawford, W.C., Carton, H., Seher, T., Combier, V., Cannat, M., Canales, J.P., Düsünür, D., Escartin, J., Miranda, J.M., 2006. Discovery of a magma chamber and faults beneath a Mid-Atlantic Ridge hydrothermal field. Nature 442, 1029–1032. https://doi.org/10.1038/nature05105

Sinton, J.M., Detrick, R.S., 1992. Mid-ocean ridge magma chambers. J. Geophys. Res. 97, 197–216. https://doi.org/10.1029/91JB02508

Small, C., 1998. Global systematics of mid-ocean ridge morphology, in: Geophysical Monograph Series. pp. 1–25. https://doi.org/10.1029/GM106p0001

Soule, S.A., Escartín, J., Fornari, D.J., 2009. A record of eruption and intrusion at a fast

spreading ridge axis: Axial summit trough of the East Pacific Rise at 9-10°N. Geochemistry, Geophys. Geosystems 10, Q10T07. https://doi.org/10.1029/2008GC002354

Soule, S.A., Fornari, D.J., Perfit, M.R., Rubin, K.H., 2007. New insights into mid-ocean ridge volcanic processes from the 2005–2006 eruption of the East Pacific Rise, 9°46′N–9°56′N. Geology 35, 1079–1082. https://doi.org/10.1130/G23924A.1

Wu, J.N., Parnell-Turner, R., Fornari, D.J., Berrios-Rivera, N., Barreyre, T., McDermott, J.M., 2023. The Role of On- and Off-Axis Faults and Fissures During Eruption Cycles and Crustal Accretion at 9°50′N, East Pacific Rise. Geochemistry, Geophys. Geosystems 24, e2022GC010794. https://doi.org/10.1029/2022GC010794

Wu, T., Tao, C., Zhang, J., Zhang, G., Zhou, J., Bin, S., 2022. Near-bottom survey of hydrothermal sulfide on an extremely magmatic accretion segment along an ultraslow-spreading ridge. Deep. Res. Part I Oceanogr. Res. Pap. 187, 103830. https://doi.org/10.1016/j.dsr.2022.103830

Yue, X., Li, H., Ren, J., Tao, C., Zhou, J., Wang, Y., Lü, X., 2019. Seafloor hydrothermal activity along mid-ocean ridge with strong melt supply: study from segment 27, southwest Indian ridge. Sci. Rep. 9, 9874. https://doi.org/10.1038/s41598-019-46299-1

Zhou, F., Dyment, J., 2023. Temporal and spatial variation of seafloor spreading at ultraslow spreading ridges: Contribution of marine magnetics. Earth Planet. Sci. Lett. 602, 117957. https://doi.org/10.1016/j.epsl.2022.117957

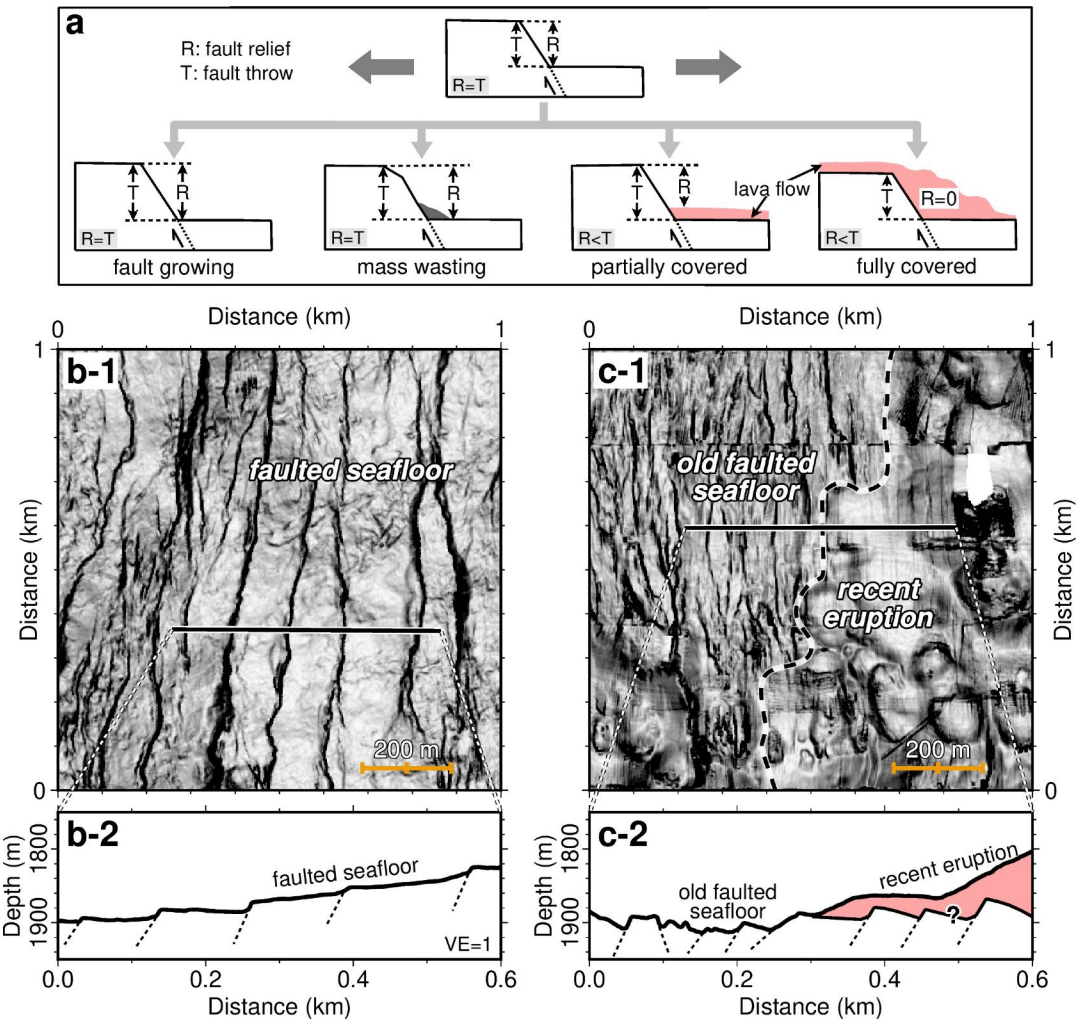

489

490 Fig. 1. **Appearance of fault scarps in young volcanic seafloor.** (a) Sketch of fault scarps
491 influenced by tectonic extension, mass wasting, and lava flow. Measurements of fault relief
492 (*R*) are provided, representing the minimum estimate of fault throw (*T*). (b-1) and (c-1)
493 Shaded high-resolution bathymetry showing faulted seafloor and fault scarps partially
494 covered by a recent eruption, respectively (See locations in Fig. 2g and 2h). Maps are in the
495 same distance scale (1×1 km^2). (b-2) and (c-2) Depth profiles with no vertical exaggeration
496 (VE=1).

497

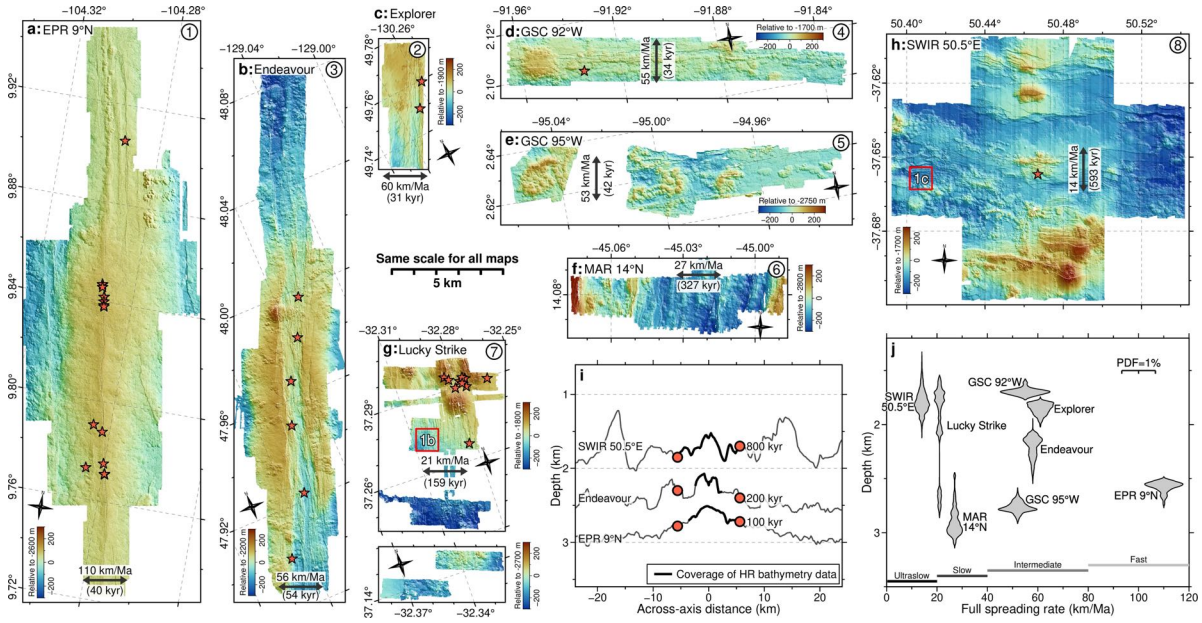

Fig. 2. **High-resolution bathymetry data of 8 study sites.** (a)-(h) Maps are in the same distance scale and the same relative color scale. See Fig. S2 for data locations, Fig. S3 for large-scale low-resolution shipboard bathymetric maps, and Table S1 for site information. Numerical labels (1-8) at the upper-right corner are sorted by spreading rate in descending order. Mean crustal ages (in brackets) are calculated by dividing the survey area by along-axis distance and general spreading rates (see Methods in Supplementary). Note that the Lucky Strike area (g) includes two panels from the segment center (upper) to the end (lower). Red squares in Fig. 2g and 2h are locations of Fig. 1b and 1c, respectively. Red stars indicate locations of hydrothermal vents. (i) Across-axis profiles of shipboard bathymetry data for the EPR 9°N, Endeavour, and SWIR 50.5°E study sites, showing the relationship between spatial and temporal scales. Thick black lines show the coverage of high-resolution bathymetry data. Red circles indicate different crustal ages at ~5.6 km off axis. (j) Violin plot showing the depth distribution of high-resolution bathymetry data at each site. The probability density function (PDF) is calculated with a spacing of 1 m. EPR: East Pacific Rise. GSC: Galapagos Spreading Center. MAR: Mid-Atlantic Ridge. SWIR: Southwest Indian Ridge.

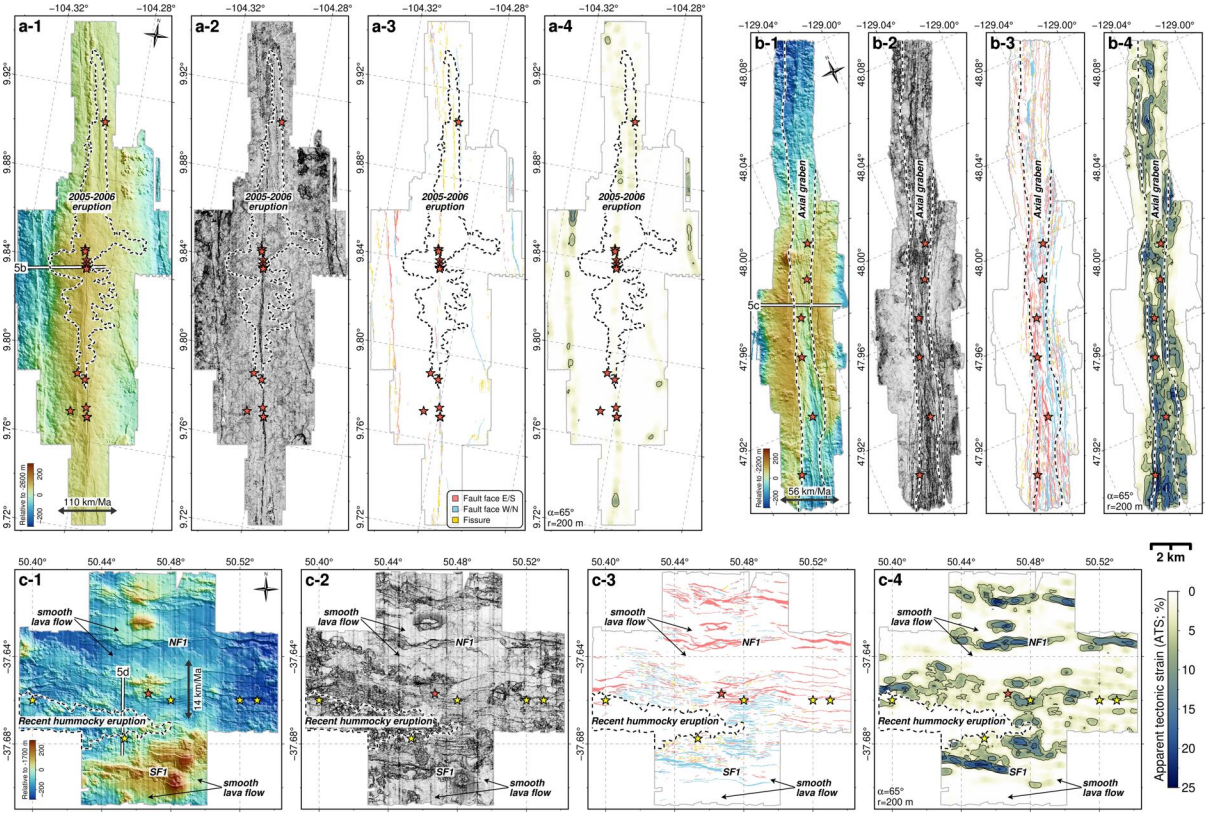

515

516 Fig. 3. **Shaded maps, faulting patterns, and apparent tectonic strain maps of the EPR**
517 **9°N (a), Endeavour (b), and SWIR 50.5°E (c) study sites.** All maps have the same distance
518 scale. White solid lines are profile locations in the upper panels of Fig. 5b-5d. Red stars
519 indicate locations of hydrothermal vents. Yellow stars in (c) indicate locations of
520 hydrothermal plume anomalies (Wu et al., 2022; Yue et al., 2019). Dashed lines represent the
521 extent of the 2005-2006 eruption (a) (Soule et al., 2007), the axial graben (b), and the recent
522 hummocky lava flows built by multiple eruptions (c) (Chen et al., 2021). NF1 and SF1 in (c)
523 are conjugate northern and southern bounding faults, respectively (Chen et al., 2021). (a-2),
524 (b-2), and (c-2) Shaded high-resolution bathymetry maps. (a-3), (b-3), and (c-3) Interpreted
525 faults and fissures. Red areas are faults facing east or south. Blue areas are faults facing west
526 or north. Orange areas are fissures. (a-4), (b-4), and (c-4) Calculated apparent tectonic strain
527 (ATS) based on interpreted faults and fissures. Color scale is the same for the three sites.
528 Fault dip and search radius are given as $\alpha = 65°$ and $r = 200$ m in the ATS calculation. Other
529 combinations of α (75°) and r (100 and 400 m) of these three sites can be found in Fig. S6-
530 S8.

531

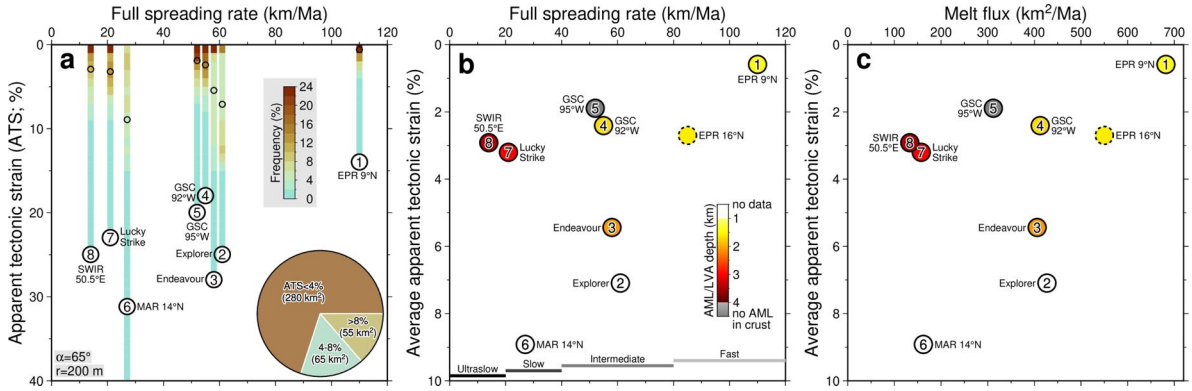

Fig. 4. **Apparent tectonic strain estimated using high-resolution bathymetry data.** (a) Range and frequency of apparent tectonic strain (ATS) of 8 study sites plotted vs. spreading rate. Vertical bars show the ATS range, and the frequency is color-coded. Small open circles mark the average ATS, also shown in (b) and (c). Fault dip and search radius are given as α = 65° and r = 200 m in the ATS calculation (see Fig. S14 for other combinations of α and r). Pie chart shows the proportion of the mapped seafloor (400 km^2 in total) at the ATS of <4%, 4-8%, and >8%. (b) Average ATS is calculated using all faults and fissures within the mapped area, except for the EPR 16°N, where average ATS is calculated by averaging ATS along five cross-axis sections (Le Saout et al., 2018). AML/LVA depth is color-coded, and see Table S1 for the compilation (Chen et al., 2023a). AML: axial melt lens. LVA: low-velocity anomaly. (c) Average ATS plotted vs. melt flux. Melt flux is the product of spreading rate and magmatic crustal thickness (Table S1).

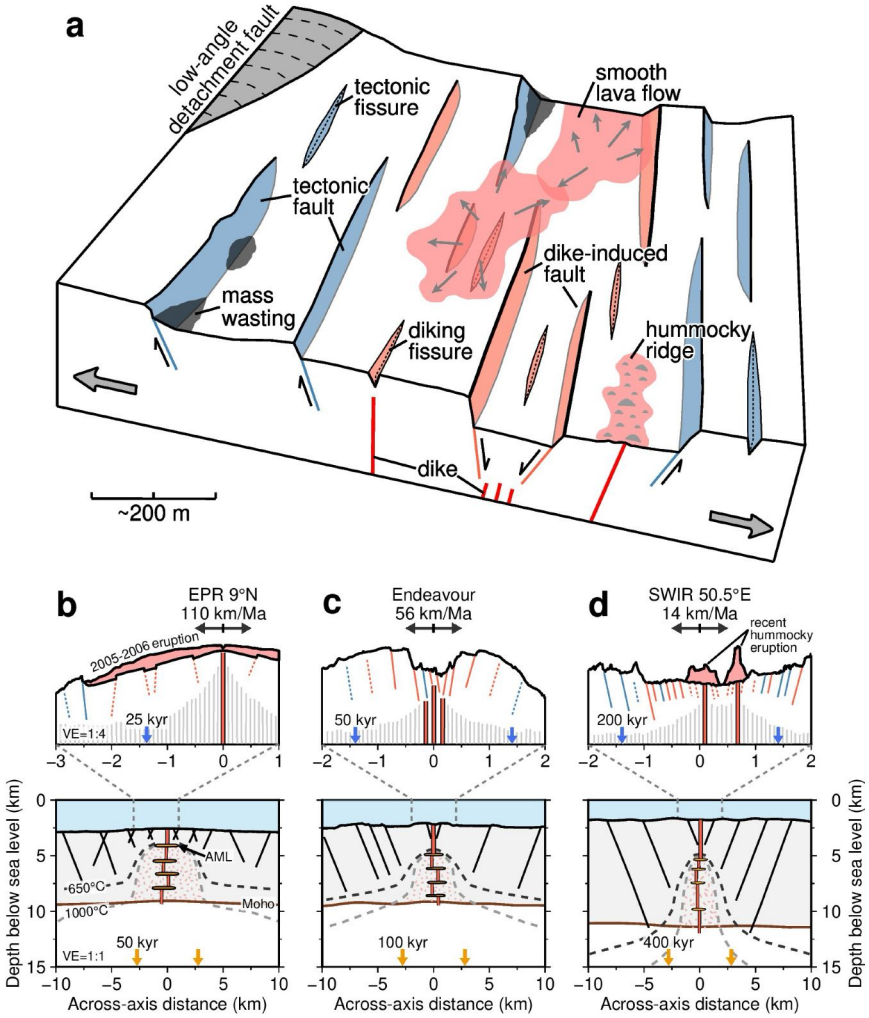

Fig. 5. **Fault synthesis in young seafloor.** (a) Sketch of the fault synthesis. Fault scarps and fissures can be induced by tectonic stretching (blue area) and dike intrusions (pink area) or covered by volcanic eruptions and mass wasting. A low-angle detachment fault is also drawn, although our data do not map it. (b)-(d) Upper panels (VE=1:4) are based on high-resolution bathymetric profiles of the fast-spreading EPR 9°N, the intermediate-spreading Endeavour, and the ultraslow-spreading SWIR 50.5°E (see profile locations in Fig. 3). Blue arrows indicate different crustal ages at ~1.4 km off axis. Vertical red and gray bars indicate active and inactive dikes, respectively. Blue and pink lines represent faults induced by tectonic stretching and dike intrusions, respectively. Dashed lines represent faults covered by lava flows. Lower panels (VE=1:1) of crustal cross-sections are constrained by seismic studies of the EPR 9°N (Detrick et al., 1987; Dunn et al., 2000; Marjanović et al., 2014), the Endeavour (Arnoux et al., 2019; Carbotte et al., 2006), and the SWIR 50.5°E (Li et al., 2015). Orange arrows indicate different crustal ages at ~2.8 km off axis. Solid black lines indicate faults. The 650°C (dashed black lines) and 1000°C (dashed gray lines) isotherms represent the base of the brittle lithosphere and the basaltic solidus, respectively. AML: axial melt lens.

562

Supplementary Information for

Fault scarps and tectonic strain in young volcanic seafloor

Jie Chen[1,2], Javier Escartin[2], Mathilde Cannat[1]

[1] Université Paris Cité, Institut de physique du globe de Paris, CNRS, 75005 Paris, France

[2] Laboratoire de Géologie, Ecole Normale Supérieure/CNRS UMR 8538, PSL Research University, Paris 75005, France

Corresponding author: Jie Chen (chen@geologie.ens.fr)

This PDF file includes:

- Text for Methods
- Table S1
- Fig. S1-S17

Text for Methods

High-resolution bathymetry data

We use AUV/ROV high-resolution (HR) bathymetry data that cover 400 km^2 of the seafloor near the axis at 8 mid-ocean ridge sites (Fig. 2). See Fig. S2 for site locations and see Fig. S3 for larger low-resolution shipboard bathymetric maps of all sites. See Table S1 for compiled information on datasets and their characteristics. One site (EPR 9°N) is fast spreading, four sites (Endeavour, Explorer GSC 95°W, and GSC 92°W) are intermediate spreading, two sites (MAR 14°N and Lucky Strike) are slow spreading, and one site (SWIR 50.5°E) is ultraslow spreading. Data resolution is 1 m, except for the Lucky Strike and the SWIR 50.5°E (2 m). All sites have volcanic-dominated seafloor, covering along-axis distances of 5-25 km and mean across-axis distance of 1.7-8.3 km. Bathymetric data are publicly available (see Data Availability).

Crustal age estimation

Crustal ages of the 8 sites are estimated by dividing off-axis distance by general spreading rates constrained by magnetics, which range between ~50 and ~940 kyr. Mean crustal ages are calculated by dividing survey areas by along-axis distance and general spreading rates, which range between ~30 and ~590 kyr (Table S1). However, this estimation introduces uncertainties, because bathymetry data provides only a snapshot of the seafloor at the time of the survey, and general spreading rates cannot accurately reflect local spreading rates in axial regions. This discrepancy is evident in subaerial spreading centers, i.e., the Dabbahu segment of the Afar rift, where the general spreading rate is <20 mm/yr, yet a transient rate reached up to 110 mm/yr during the 2005-2010 dike intrusion (Pagli et al., 2014). Additionally, seafloor age may be overestimated due to recent lava flows that can cover extensive areas of the seafloor, e.g., the 2005-2006 eruption at the EPR 9°N (Soule et al., 2007).

Faults and fissures detection

HR bathymetry and calculated slope maps are used to detect faults and fissures by a single analyst (J.C.), with a procedure discussed and agreed upon with the other authors. Parts of the picked faults and fissures are adapted from previous studies at the SWIR 50.5°E (Chen et al., 2021), the Explorer (Deschamps et al., 2007), and the EPR 9°N (Wu et al., 2023). The difference from most of the previous studies is that we digitize closed polygons of fault tops and bottoms and fissure margins, rather than only fault tops or fissure centers. In Fig. S1, we show an example within a 1×1 km^2 area of the Lucky Strike (location: red square

in Fig. 2g), and in Data Availability, we provide a screen record of an example showing the picking process of faults and fissures within this example area. Fault scarps are linear and correspond to sharp changes in bathymetry and slope at their upper and lower limits. Fissures correspond to linear depressions (width from a few m to <50 m typically). This fault-fissure detection, applied to the 8 study sites with HR bathymetry data, yields 6413 faults (1589 km in length) and 2775 fissures (244 km in length) in total (see Table S1).

Fault relief

Fault relief (R) is defined as the depth difference between the top and the bottom of the fault scarp. This measurement represents a minimum estimate of fault throw (T), with discrepancies from factors such as mass wasting, lava flow coverage (e.g., Fig. 1) and block rotation (Karson et al., 1992), which cannot be resolved using bathymetry data alone. We measure the fault relief based on cross-axis transects spaced at 2 m. At all spreading rates, previous studies report that the cumulative frequency of the fault relief follows an exponential law (Carbotte and Macdonald, 1994; Chen et al., 2021; Deschamps et al., 2007; Escartín et al., 1999; Le Saout et al., 2018). This distribution can be used to verify if the picking process and the measurement record small fault scarps. For our 8 study sites, we show the maximum fault relief versus cumulative frequency in log-linear plots, indicating that they all follow exponential laws with R^2 at 0.9626-0.9875 (Fig. S4).

Fault dip

Fault dip (α) is defined as the largest value along the fault scarp, as it could be sharply decreased at the scarp bottom by the presence of lava flows and/or mass wasting after faulting (Fig. 1a). The fault dip is measured based on cross-axis transects spaced at C = 2 m, accompanying with the measurement of fault throw. We plot all measured fault dips and the median value of the fault dip versus fault throw for 8 study sites (Fig. S5). The median values of the fault dip increase from 20° to 60-75° as the fault throw increases from 0 to 50 m, and dips stabilize on 60-75° at throws of >50 m. The maximum fault dip, especially for small faults, could be underestimated due to the data resolution, compared with ground truths by submarine videos (Wu et al., 2023). In our treatments, we consider uniform median dips of 65° and 75° for estimating apparent tectonic strain.

Label	1	2	3	4	5	6	7	8
Site name	EPR 9°N	Explorer	Endeavour	GSC 92°W	GSC 95°W	MAR 14°N	Lucky Strike	SWIR 50.5°E
Spreading rate (km/Ma)	110	60	56	55	53	27	21	14
Area (km^2)	112.2	9.6	70.5	27.6	27	19.4	23	109.8
Max. age (kyr)	72	49	91	39	56	353	312	942
Mean age (kyr)	40	30.9	54	33.5	42	326.6	158.7	592.9
Mean depth (m)	2574	1853	2206	1697	2766	2899	2005	1787
Resolution (m)	1	1	1	1	1	1	1-2	2
Vehicle type	AUV	AUV	AUV	AUV	AUV	AUV	AUV/ROV	AUV
Data collected year	2018-2021	2002	2011	2010	2010	2018	2006-2009	2016
No. picked faults/fissures	410/733	325/93	1920/626	547/372	466/128	630/317	762/247	1343/259
Cumu. length of faults/fissures (km)	109/55	87/11	536/62	118/41	92/12	126/26	149/16	372/21
Mean fault spacing (m)	577	71	82	98	223	147	110	238
Average ATS at α=65° (%)	0.59	7.1	5.4	2.4	1.9	8.9	3.2	2.9
Previously estimated ATS (%)	0.15-0.23	6-9	-	-	-	-	-	3.6-5.1
Crustal thickness (km)	6.2	7 (assumed)	7	7	6	6 (assumed)	7.5	9.5
AML/LVA depth (km)	1.3-2	No data	2.1-3.3	1.4-2.4	No AML in crust	No data	3-3.8	3.5-4.2 (LVA)

Table S 1. **Information of high-resolution bathymetry data for the 8 study sites.** Locations are shown in Fig. S2. Compilation of seismically-imaged crustal thicknesses and AML/LVA depths is taken from (Chen et al., 2023a), except the crustal thicknesses at the Explorer and the MAR 14°N that have not been measured and assumed here as 7 and 6 km, respectively. ATS: apparent tectonic strain. AML: axial melt lens. LVA: low-velocity anomaly.

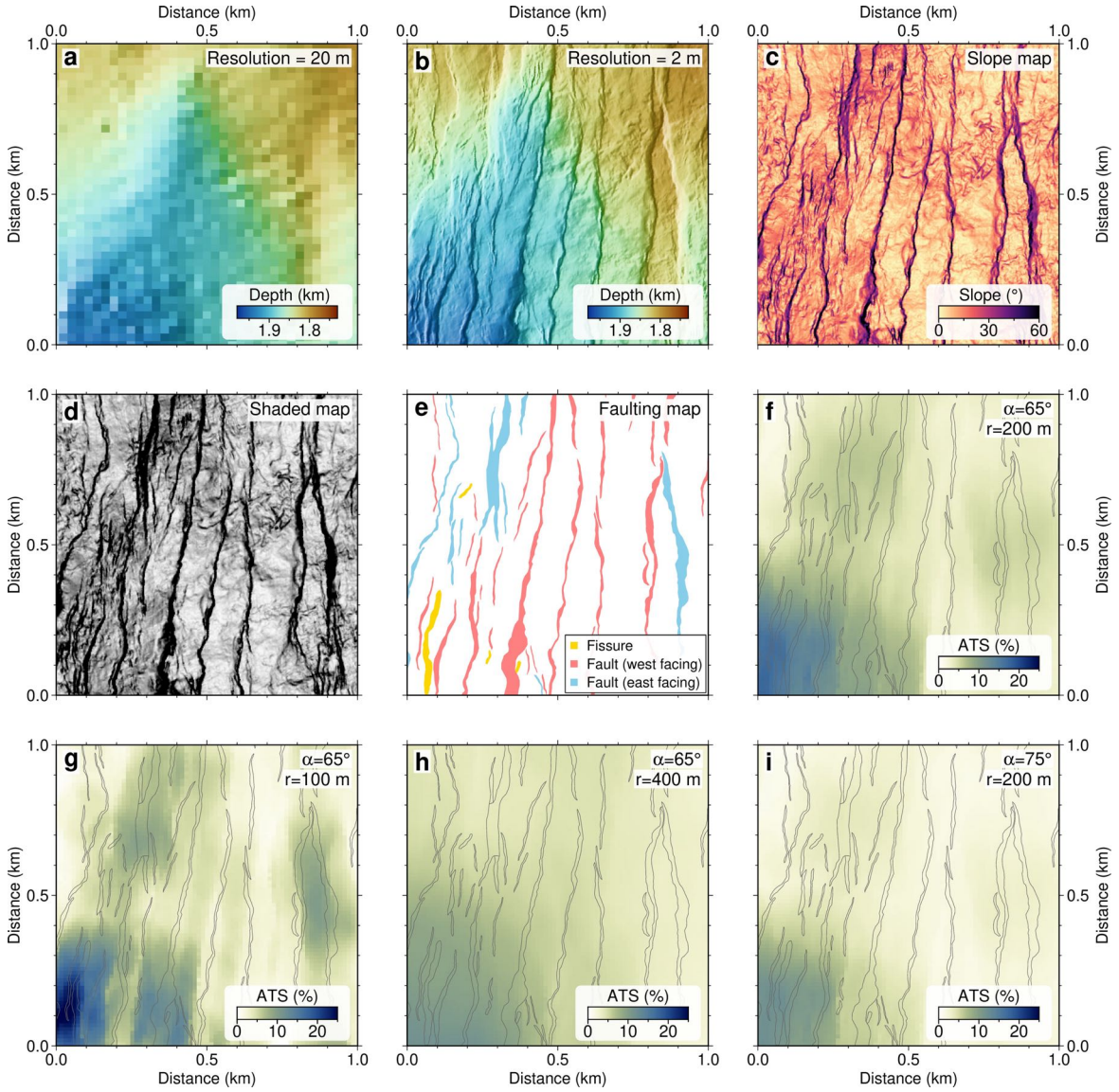

Figure S 1 | **Example of a 1×1 km² area for fault detection and the quantification of apparent tectonic strain.** See the location in Fig. 2g (Lucky Strike). (a) Low-resolution (20 m) shipboard bathymetry map. (b) High-resolution (2 m) bathymetry map. (c) Slope map derived from high-resolution bathymetry map. (d) High-resolution shaded map. (e) Detected faults and fissures. See Video S1 for the screen record of the picking process within this area. (f) Calculated apparent tectonic strain (ATS) based on detected faults and fissures. Fault dip and search radius are given as $\alpha = 65°$ and $r = 200$ m. (g) ATS calculated using $\alpha = 65°$ and $r = 100$ m. (h) ATS calculated using $\alpha = 65°$ and $r = 400$ m. (i) ATS calculated using $\alpha = 75°$ and $r = 200$ m.

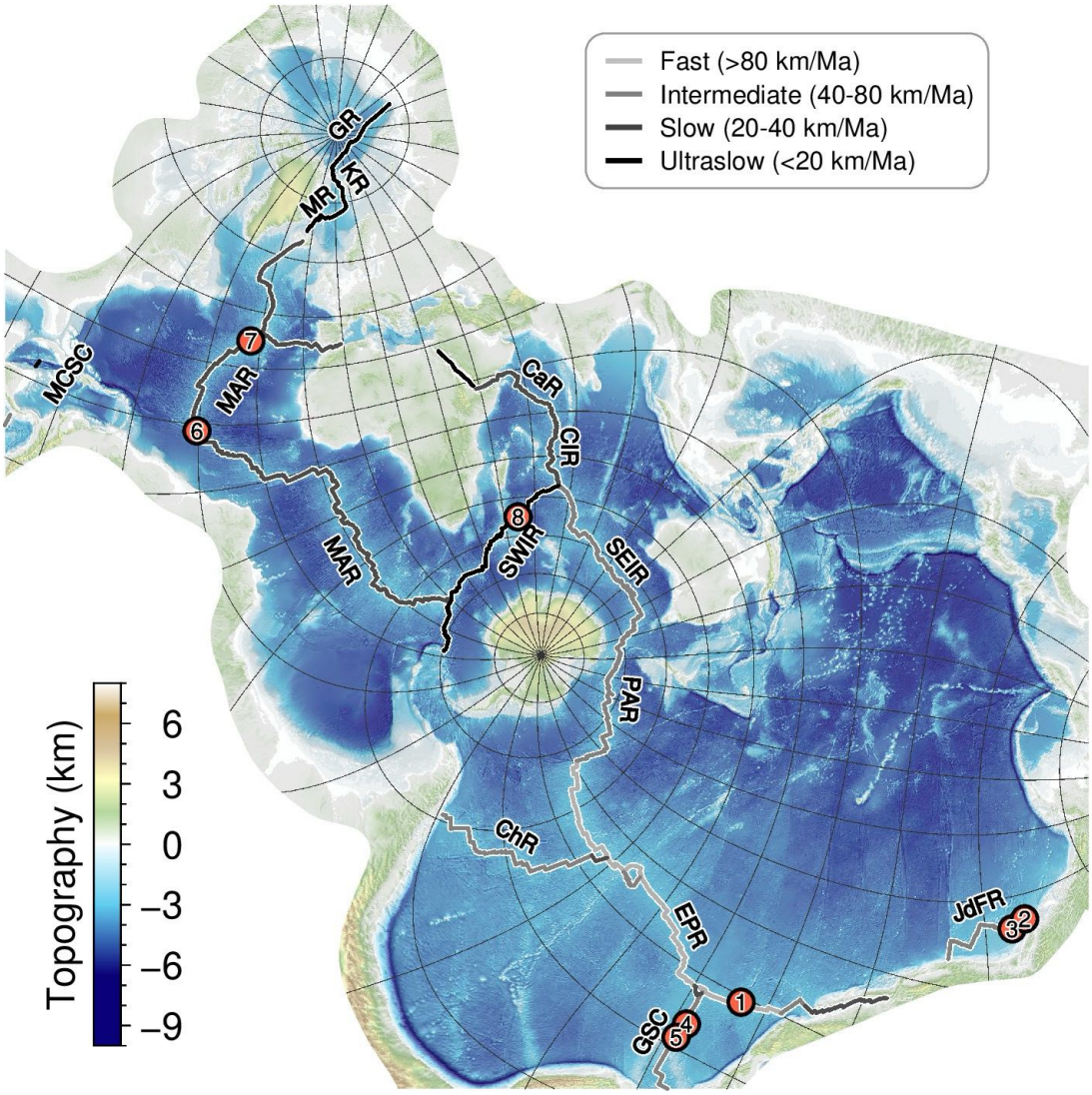

Figure S 2 | **Spilhaus world ocean map showing the 8 study sites and Mid-Ocean Ridges** (Chen et al., 2023b)**.** Red circles with numerical labels are the locations of the 8 study sites. CaR: Carlsberg Ridge, ChR: Chile Ridge, CIR: Central Indian Ridge, EPR: East Pacific Rise, GR: Gakkel Ridge, GSC: Galapagos Spreading Center, JdFR: Juan de Fuca Ridge, KR: Knipovich Ridge, MAR: Mid-Atlantic Ridge, MCSC: Mid-Cayman Spreading Center, MR: Mohns Ridge, PAR: Pacific-Antarctic Rise, SEIR: Southeast Indian Ridge, SWIR: Southwest Indian Ridge.

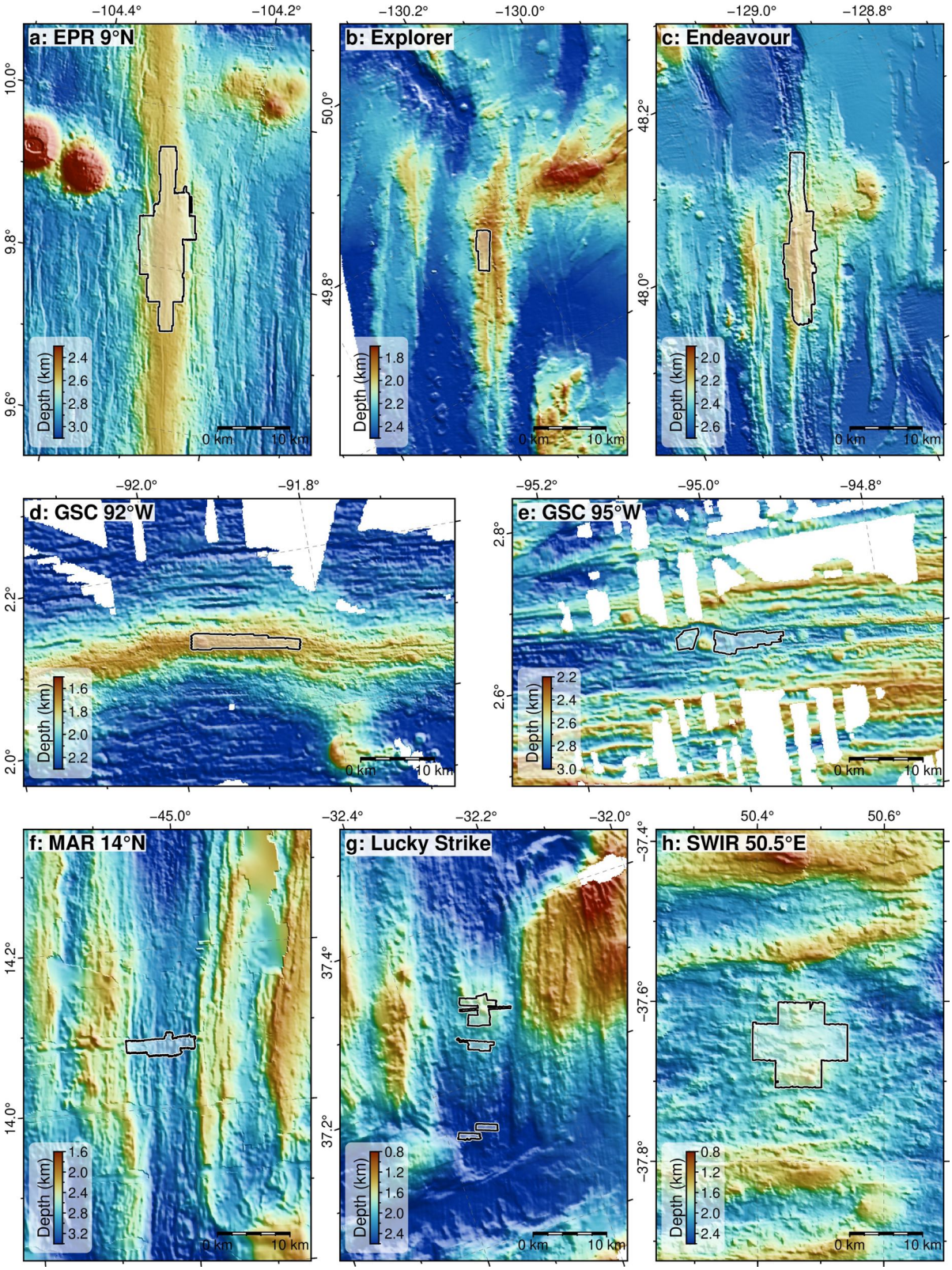

Figure S 3 | **Low-resolution shipboard bathymetry maps showing large-scale backgrounds of the 8 study sites**. Polygons show AUV-mapped seafloor in Fig. 2. Maps are in the same distance scale. Bathymetry data are downloaded from https://www.gmrt.org/.

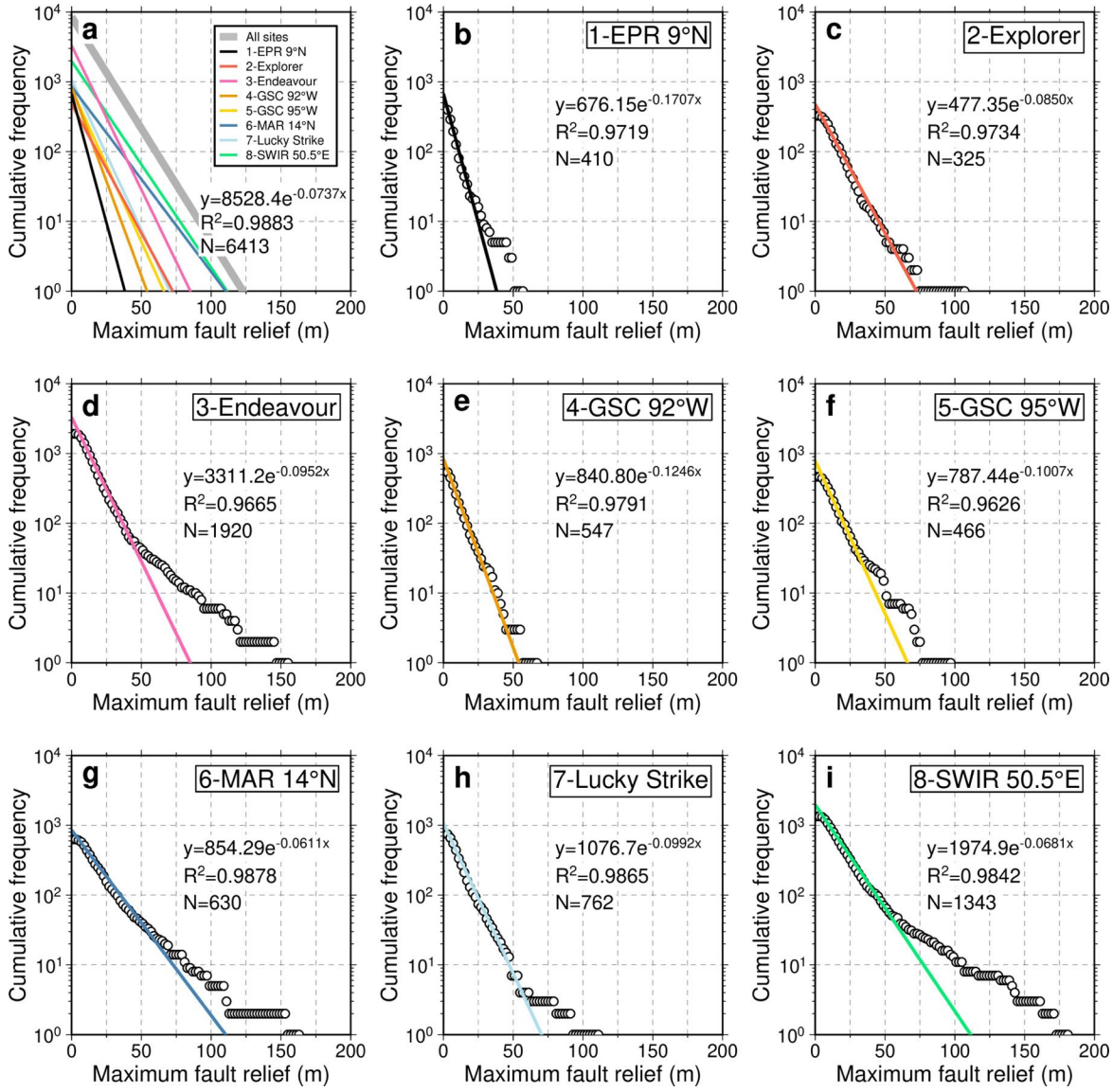

Figure S 4 | **Cumulative frequency of maximum fault releif for the 8 study sites, plotted in log-linear relationship.** Bin is 2 m. Fault numbers (N) are indicated. Exponential fits are indicated with R^2 at 0.9626-0.9878. (a) Integration of exponential fits.

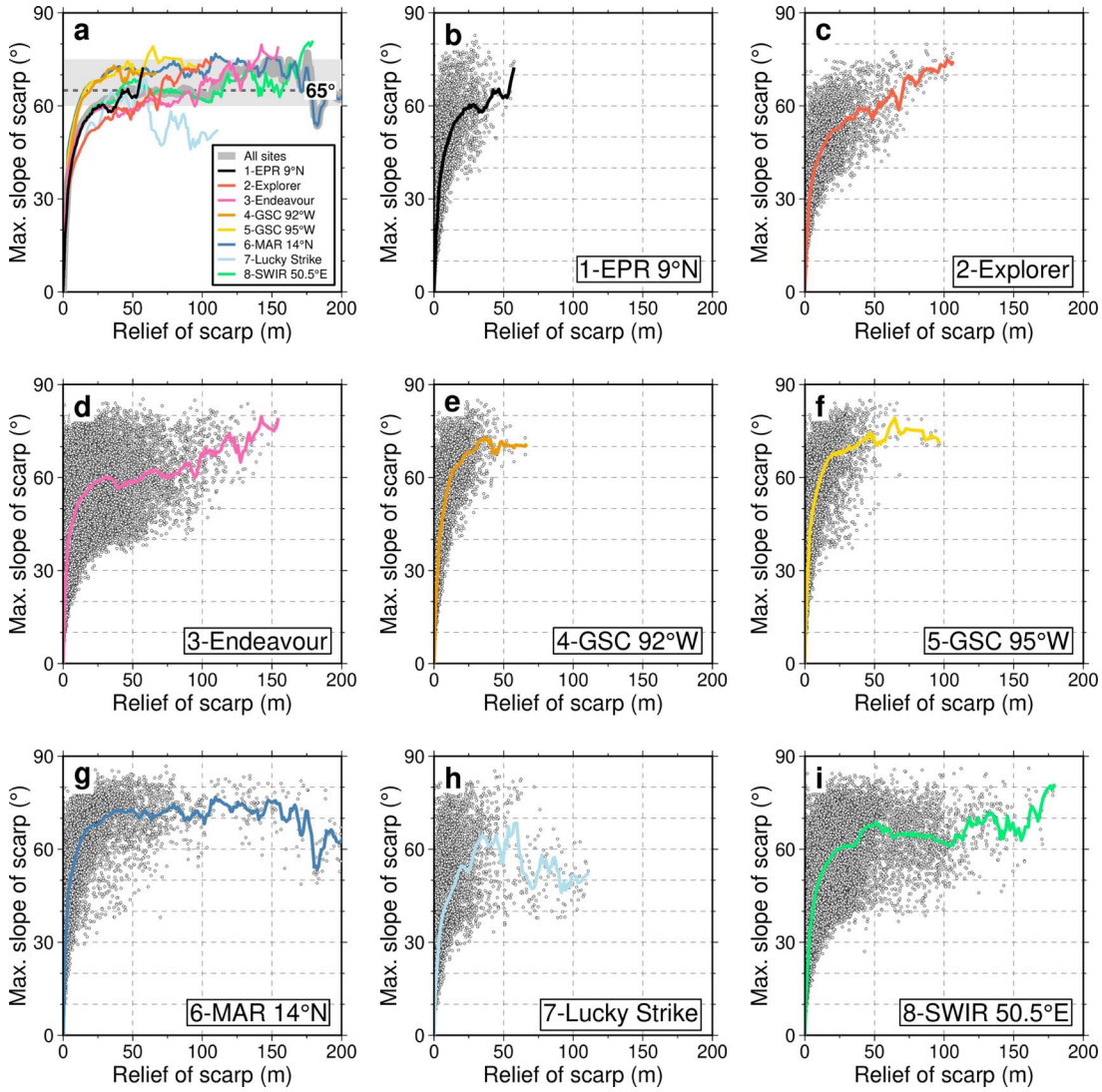

Figure S 5 | **Measured fault dip (dots) and median of fault dip (lines) versus fault releif for the 8 study sites.** (a) Integration of the median of fault dip, which stabilizes on 60-75° at throws of >50 m.

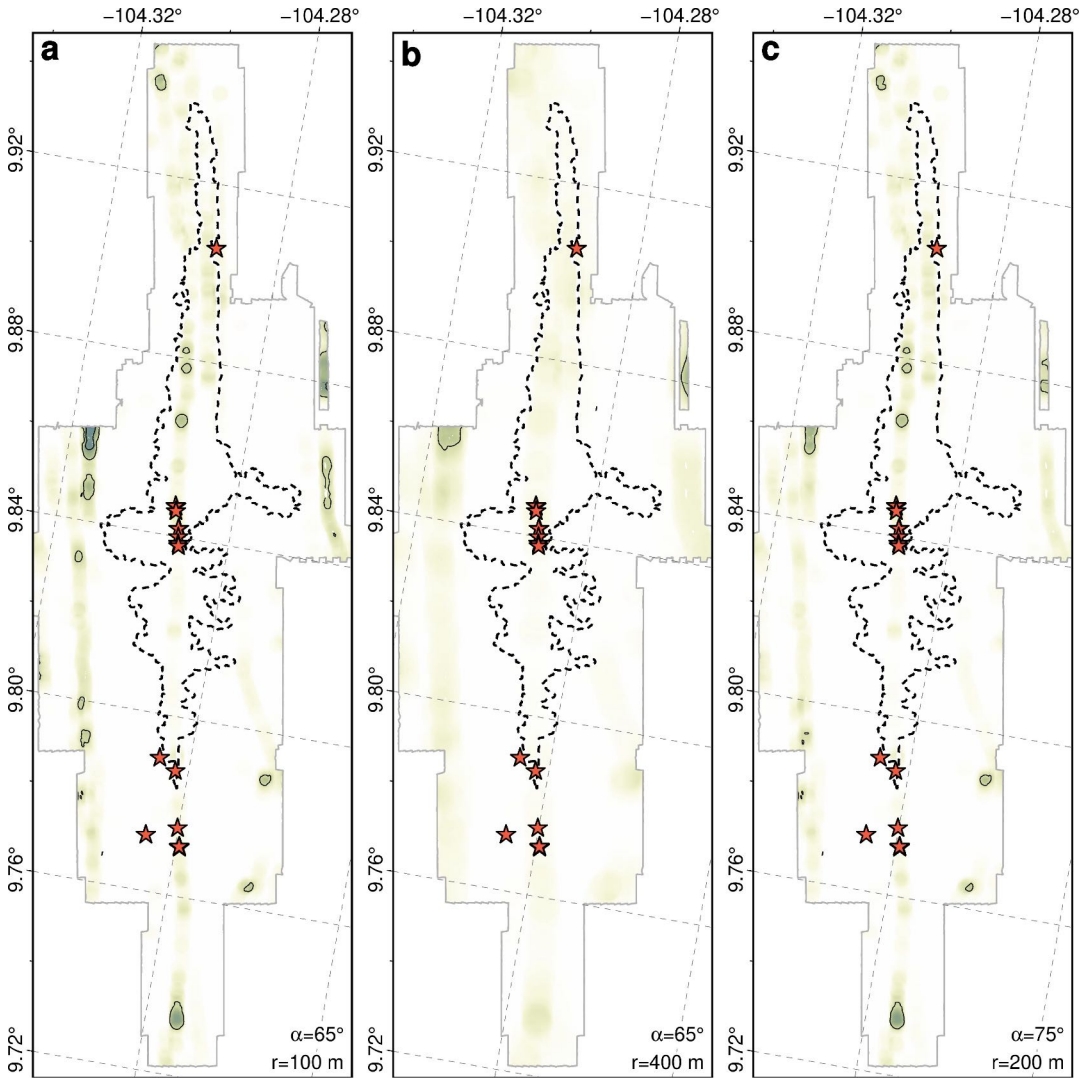

Figure S 6. Apparent tectonic strain calculated using α = 65/75° and r = 100/200/400 m of the EPR 9°N. See the combination of α = 65° and r = 200 m in Fig. 3. See the color scale in Fig. 3 (same below in Fig. S7-S13).

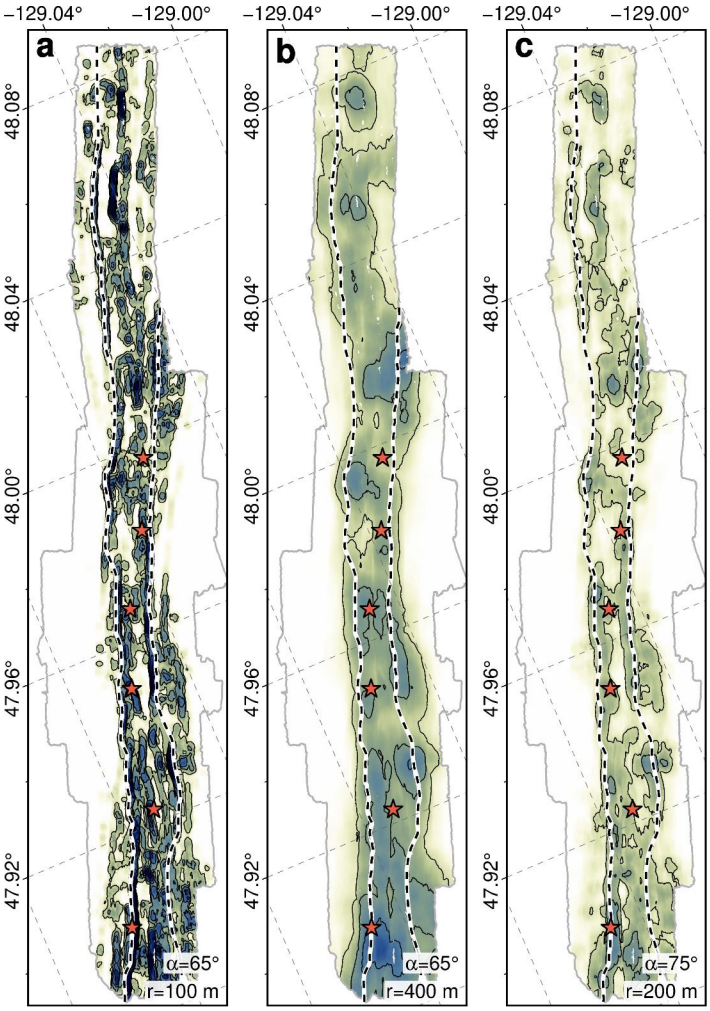

Figure S 7. Apparent tectonic strain calculated using α = 65/75° and r = 100/200/400 m of the Endeavour.

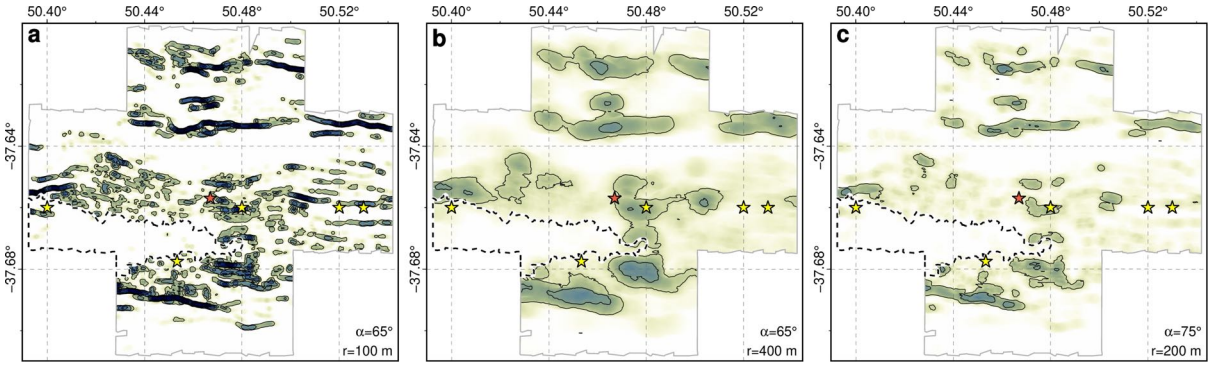

Figure S 8. Apparent tectonic strain calculated using α = 65/75° and r = 100/200/400 m of the SWIR 50.5°E.

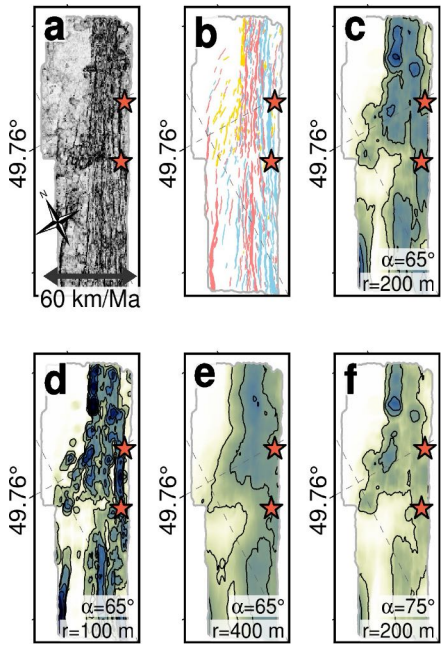

Figure S 9. Shaded map, faulting pattern, and apparent tectonic strain of the Explorer.

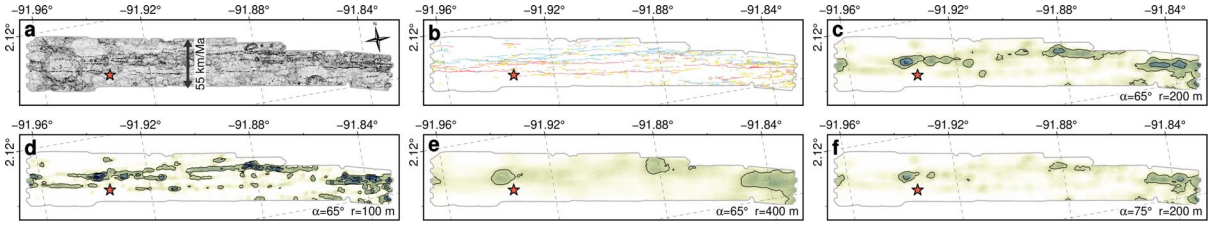

Figure S 10. Shaded map, faulting pattern, and apparent tectonic strain of the GSC 92°W.

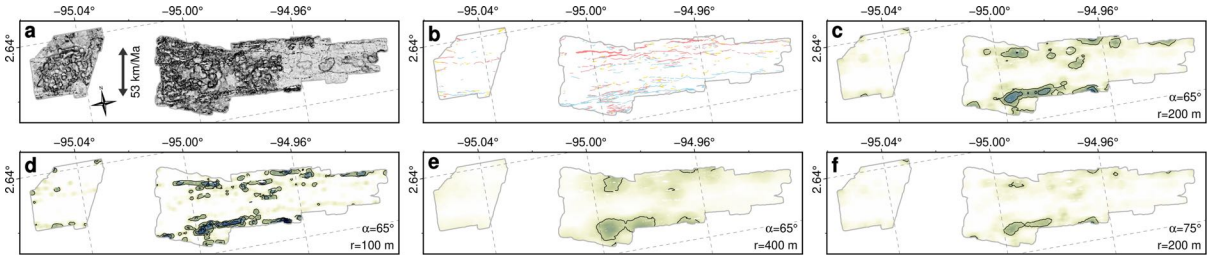

Figure S 11. Shaded map, faulting pattern, and apparent tectonic strain of the GSC 95°W.

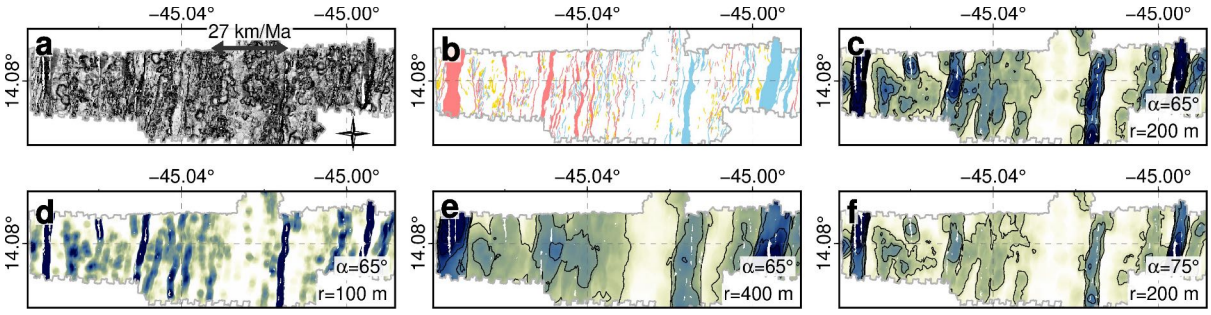

Figure S 12. Shaded map, faulting pattern, and apparent tectonic strain of the MAR 14°N.

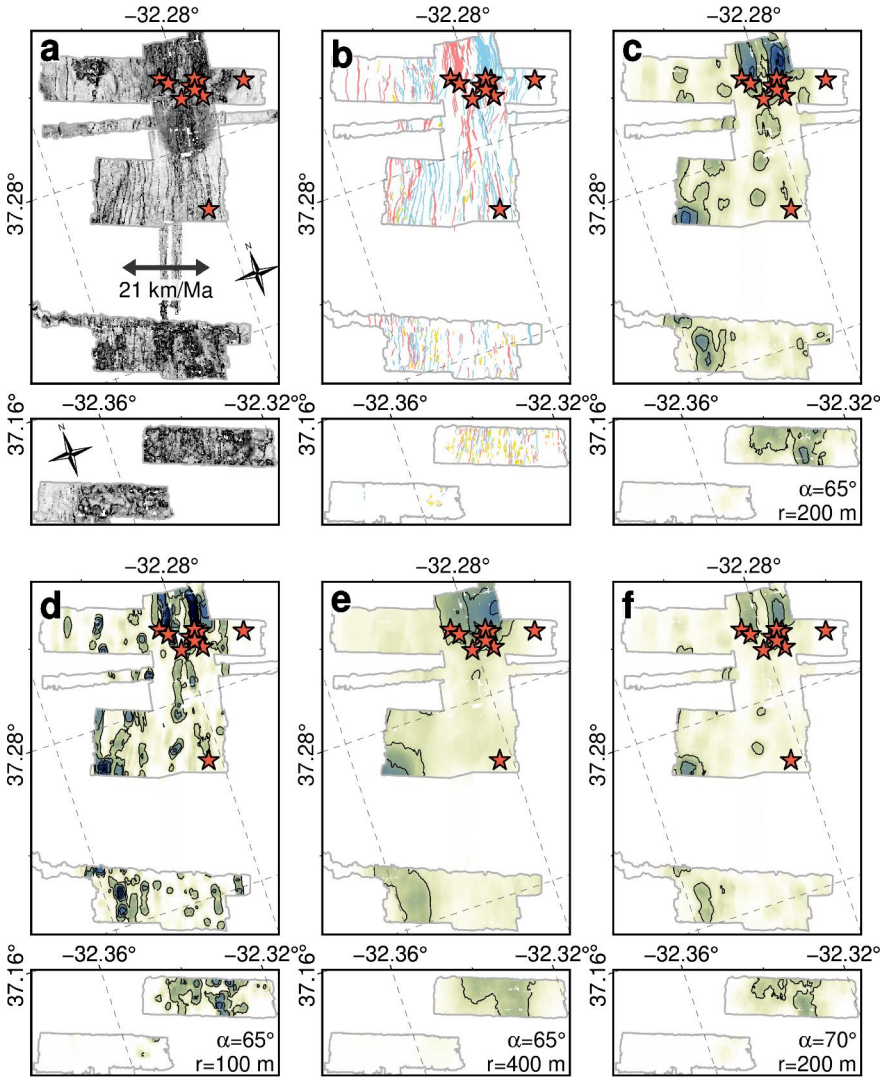

Figure S 13. Shaded map, faulting pattern, and apparent tectonic strain of the Lucky Strike.

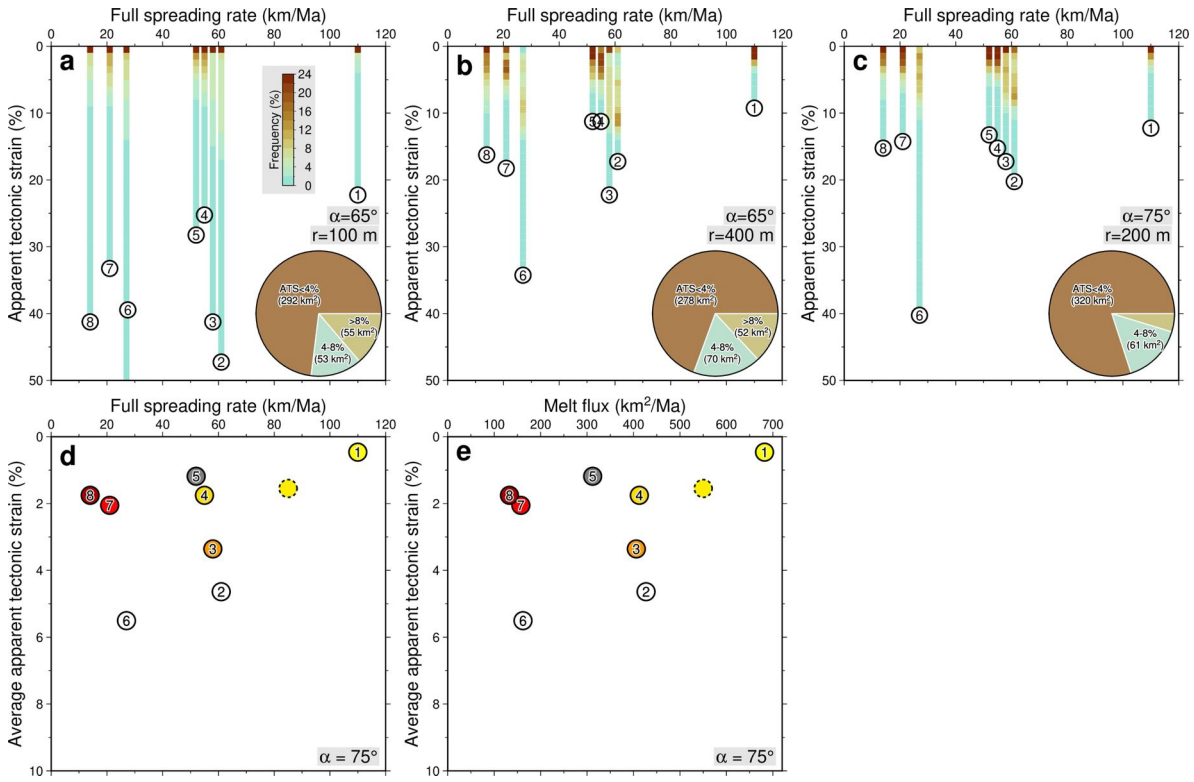

Figure S 14. Apparent tectonic strain with α = 65/75° and r = 100/200/400 m plotted vs. spreading rate and melt flux. See the combination of α = 65° and r = 200 m in Fig. 4.

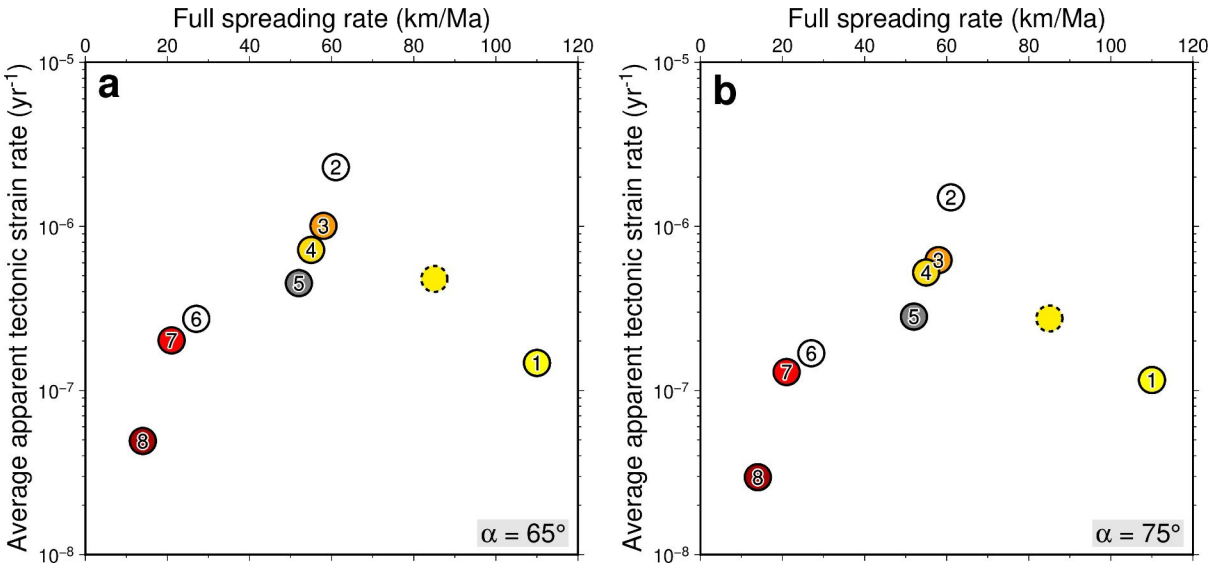

Figure S 15. Average apparent tectonic strain rate, estimated by dividing average ATS by mean crustal ages. The average ATS rate is highest at the intermediate-spreading ridges, decreasing towards fast- and slow-spreading ridges by 1-2 orders of magnitude. Note that many uncertainties should be considered in this estimate, particularly those arising from the inherited use of general and uniform spreading rates in axial regions.

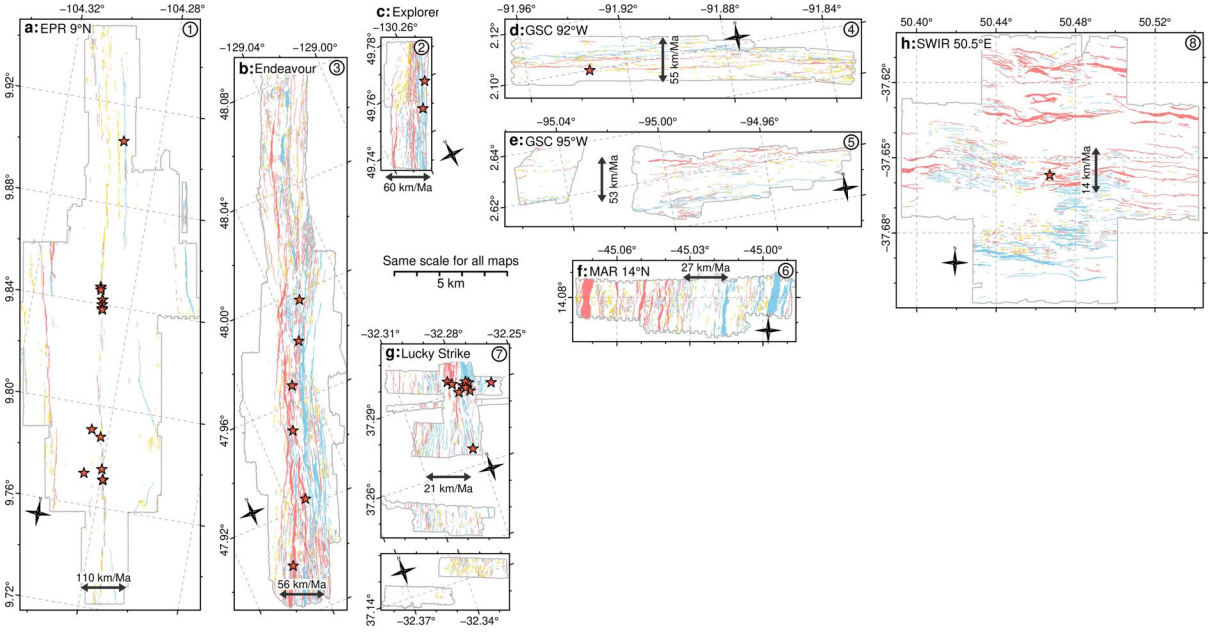

Figure S 16. Maps of faulting patterns of the 8 study sites. Maps are in the same distance scale. Red areas are faults facing east or south. Blue areas are faults facing west or north. Orange areas are fissures.

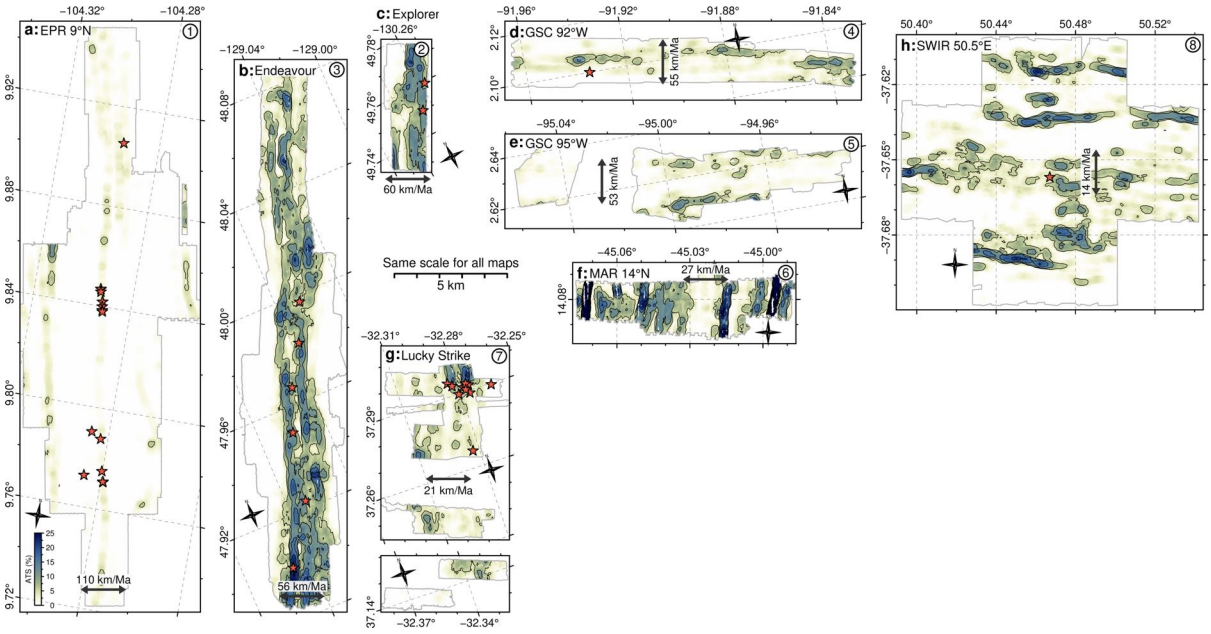

Figure S 17. Apparent tectonic strain of 8 study sites. Maps are at the same distance and on the same color scales. Fault dip and search radius are given as $\alpha = 65°$ and $r = 200$ m in the calculation of apparent tectonic strain (ATS).

Additional references

Chen, J., Zhang, T., Tominaga, M., Escartin, J., Kang, R., 2023b. Ocean sciences with the Spilhaus projection: a seamless ocean map for spatial data recognition. Sci. Data 10, 410. doi:10.1038/s41597-023-02309-6.

Karson, J.A., Hurst, S.D., Lonsdale, P., 1992. Tectonic rotations of dikes in fast-spread oceanic crust exposed near Hess Deep. Geology 20, 685–688. doi:10.1130/0091-7613(1992)020<0685:TRODIF>2.3.CO;2.

Pagli, C., Wang, H., Wright, T.J., Calais, E., Lewi, E., 2014. Current plate boundary deformation of the Afar rift from a 3-D velocity field inversion of InSAR and GPS. J. Geophys. Res. Solid Earth 119, 8562–8575. doi:10.1002/2014JB011391.